

Numerical investigation of transient hydrothermal processes around intrusions: heat transfer and fluid circulations leading to mineralization patterns.

Khalifa Eldursi¹, Yannick Branquet^{1*}, Laurent Guillou-Frottier², Eric Marcoux¹

1. Université d'Orléans et Université François Rabelais de Tours / CNRS / INSU, ISTO - UMR 6113, Campus CNRS, 1A rue de la Férollerie, 45071 Orléans Cedex, France.

2: Bureau de Recherches Géologiques et Minières, 3 avenue Claude Guillemin, BP36009, Orléans, F45060, Cedex2, France.

*Corresponding author: Yannick.Branquet@univ-orleans.fr

Résumé et conclusion français du chapitre (III)

1. Résumé

Les circulations de fluides autour des intrusions magmatiques ont été évaluées par modélisation numérique couplant circulation de fluide et transfert de chaleur. Ce travail rend compte de modèles physiques simples qui ne simulent pas i) les fluides polyphasés ; ii) la diffusion chimique, iii) la topographie, iv) l'entrée dans le système d'eaux météoriques ou magmatiques. Néanmoins, l'originalité de notre modélisation par rapport aux travaux préexistants repose sur les points suivants : i) la perméabilité varie de façon continue avec la profondeur (loi puissance) ; ii) les modèles ont été élaborés en tenant en compte de la période de mise en place de l'intrusion ; iii) un nouvel index de probabilité de précipitation minérale a été établi et cartographié sur les modèles (R^2AI) ; iv) de nombreuses situations géologiques naturelles ont été testées. Elles présentent des différentes profondeurs d'emplacement, des zones de perméabilité élevée (auréoles thermiques fracturées, failles), ainsi que des géométries de pluton complexes avec des apex ; v) la zone en dessous de pluton a été explorée.

Nos résultats principaux sont :

1. L'hydrodynamique ainsi que la zone favorable de minéralisation autour du pluton sont fortement dépendants de la profondeur de mise en place du pluton. Les plutons mis en place en profondeur (dessous 10km) et non liés aux zones de perméabilité élevée (i.e. failles) n'induisent pas d'advection efficace pour former des zones minéralisées. Au-dessus de 4.5 km de profondeur, le seuil de perméabilité de 10^{-16} m^2 est atteint et les cellules convectives du second ordre peuvent créer des zones additionnelles de décharge focalisée de fluide où des minéralisations sont potentiellement présentes.
2. Pour toutes les profondeurs d'emplacement, la zone en dessous du pluton ne présente pas de potentiel de minéralisation.
3. Les apex plutoniques modifient fortement l'hydrodynamique autour de l'intrusion en focalisant et relocalisant des zones advectives de décharge probablement minéralisantes autour d'eux. Cette relocalisation a tendance à enlever ou restreindre les zones favorables autour du pluton principal.
4. La phase de refroidissement n'est pas nécessairement la phase convective principale lors de la mise en place d'un pluton de grande dimension. En effet, la zone advective principale la plus large et efficace pour dissiper la chaleur peut également se produire avant et pendant la phase la plus chaude de l'emplacement (i.e. avant que le magma ne

crystallise complètement). Ce résultat doit être pris en compte pour interpréter les datations absolues dans de tels systèmes (âge de mise en place de l'intrusion, du refroidissement, de la minéralisation).

5. En contexte extensif, les détachements sont à même de délocaliser et fortement modifier l'hydrodynamique induite par la mise en place d'un pluton syn-tectonique. Il paraît donc surprenant, que dans ces systèmes extensifs où aucune surpression fluide n'est nécessaire pour créer des sites dilatants, si peu de gisements soient reportés dans la littérature internationale.
6. Les conditions physiques favorables pour la minéralisation sont atteintes autour de plutons mis en place dans la croûte moyenne, pendant une durée courte centrée sur la phase la plus chaude de l'intrusion. Nous proposons que, même si les arguments chimiques sont absents pour démontrer un rôle génétique de l'intrusion, la circulation de fluides induite par la seule mise en place de magma, joue un rôle fondamental dans la genèse des gisements d'or associés aux intrusions. En ce sens, le lien génétique entre intrusion et minéralisation est fort. Par ailleurs, la formation de ce type de gisements aurifère est grandement favorisée par l'occurrence d'une auréole thermique fracturée autour de l'intrusion.

Abstract

Fluid circulations around magmatic intrusion have been re-estimated through coupled hydro-thermal numerical modeling. New insights were obtained based on: i) a continuous variation of permeability with depth; ii) transient models taking into account the emplacement period of intrusion, iii) testing the physical likelihood of ore deposition using a restricted rock alteration index, iv) comparing our results with well-constrained natural cases where different emplacement depths, high permeability zones (cracked thermal aureoles), faults and plutonic apices are accounted for, v) the pluton floor has been explored.

We show that the emplacement depth is a key physical parameter controlling the extent and geometries of advective heat dissipation zones. The apices strongly modified the fluid flow pattern by focusing convective fluids and mineralization zones around them. The cooling phase is not the main phase of convection which is often associated with long-lived magma emplacement. Major advective heat dissipation and mineral deposition zone may also occur before and during the hottest phase of emplacement (before magma crystallization). Comparison with natural cases shows that we reproduced successfully in space and time the physical conditions required for mineral deposition. In particular, extensional detachments are able to delocalize and strongly modify classical fluid flow pattern induced by coeval intrusion. Finally, we conclude that, even if chemical arguments are absent, convections induced by granite emplacement play an important role in the genesis of granite-related Au deposits. Moreover, formation of this type of deposit is promoted and controlled by the occurrence of a fractured thermal aureole around the intrusion.

Keywords: Hydrothermal processes, Numerical modeling, magmatic intrusion, permeability-depth curve, mineralization, rock alteration index.

1. Introduction

Fluid flow around plutons has been extensively studied, traced and modeled within contact aureoles. Hydrodynamics around intrusions has also been assessed through 2D heuristic and finite element modeling, where heat transfer, mass transport and chemical alteration are dominant processes. Spatial distribution of ore deposits around plutonic rocks reveal particular interactions between heat transfer and fluid flow near and within contact aureoles (e.g. Gow et al., 2002). However, circulation of hot and variably pressurized fluid in the first upper kilometers of the crust is not easily predictable since rock and fluid properties may show large and time- or depth-dependent variations within such geological systems. For instance, ongoing deformation reduces effective stress and mineral reactions which are susceptible to change the host rock permeability during metamorphism (Cui et al., 2001). Thus, transient phenomena have to be considered when fluid flow around plutons is investigated.

The host rock permeability presents a threshold from which heat dissipation during cooling of the system is achieved by fluid advection rather than by conduction. Values of this threshold for homogenous country rocks span a 10^{-16} - 10^{-18} m² interval (Norton and Knapp, 1977; Norton and Knight, 1977; Gerdes et al., 1998; Cui et al., 2001), which is easily reached at a few kilometers depth (e.g. Ingebritsen and Manning, 1999). Moreover, hot plutons create density gradients and induce long-lived ($>10^5$ years after rapid magma emplacement) large-scale regional flows in the country rocks (Cathles, 1977; Norton and Knight, 1977; Cook et al., 1997). As a consequence, it was suggested that these heated fluids are responsible for development of large convective cells around the intrusion. Norton and Knight (1977) quantified a very large amount of fluid involved in convective cells far from the pluton. Expulsion of magmatic brines from intrusion increases fluid salinities and thus enhances buoyancy forces. However, production of magmatic and metamorphic fluids constitutes a pressure-driven force that interacts with buoyancy forces. Taking into account the fluid production, models of Hanson (1992), Hanson (1995) and Manning and Ingebritsen (1999) show that below a critical permeability threshold of 10^{-16} m², fluid production forces trigger supra-hydrostatic fluid pressures and dominate density-driven forces.

Sophisticated numerical models integrating fluid production, layered and transient permeabilities during chemical reaction emphasize the complexity and the partitioning of the flow pattern (Cui et al., 2001). This complex pattern of flow is confirmed by works on metamorphic mineral reactions and stable light isotopes distribution around natural aureoles (Ferry and Dipple, 1992; Nabelek and Labotka, 1993; Dipple and Ferry, 1996; Ferry et al.,

1998; Ferry et al., 2002; Rossetti et al., 2007). Controversial 1D models derived from some of these studies have a difficulty to trace peri-plutonic transient flow patterns in detail.

Regional metamorphic fluid flow and large scale structures (i.e. folds, faults, regional cleavage, etc) are considered to be first order controls on a bulk flow pattern, plutons acting only as second-order perturbations (e.g. Stern et al. 1992; Wing and Ferry, 2002). Nevertheless, second-order perturbations (i.e. anomalies) of fluid flow patterns are precisely assumed to be important factors during ore deposits genesis. Indeed, since pioneering works of De Launay (1913) to recent studies and syntheses, the role of magmatic intrusions as active agent during ore and raw materials depositing processes has been demonstrated (e.g. Sillitoe, 1991; Thompson and Newberry, 2000; Lang and Baker, 2001; Cerny et al., 2005). However, the contribution of intrusion on ore deposition is very different according to the types of deposits. We distinguish for instance: i) a strong contribution characterized by a genetic link between chemistry and mineralogy of intrusion and ore (e.g. Ni-Cu sulphide deposits within mafic-ultramafic magmas, Arndt et al., 2005); ii) a medium contribution, where it is well-established that a part of mineralizing fluids derived from the magmas (e.g. Au-Cu-Mo porphyries, Seedorf et al., 2005); iii) a limited and/or indirect contribution in which chemistry arguments for a magmatic connection are lacking or are equivocally established. For example, non-porphyry intrusion-related Au-Sn deposits present very subtle links with magmatic fluids (Thompson et al., 1999). However, even if a chemical genetic link between magma and ore is not obvious for this last class of deposits, absolute dating, spatial distribution and structural controls argue for a strong physical and/or rheological control of the intrusion on ore forming processes. Particularly, the thermo-mechanical anomaly generated by the intrusion emplacement appears to be a key factor triggering required fluid flows and mixing from different sources (magmatic, metamorphic, basinal, and meteoric). For example, genetic links between ash-flow calderas (related to a deeper magmatic source) and associated epithermal ore deposits were often debated. Guillou-Frottier et al. (2000) have however suggested that heat flow anomalies and increased fracture density at caldera margins - where epithermal ore deposits are clustered can be explained by particular thermo-mechanical processes occurring before, during and after caldera formation. Thus, heat transfer and fluid flows around magmatic intrusions appear to be of major importance in studying intrusion-related ore deposits (e.g. Cathles, 1981; Gow et al., 2002; Driesner and Geiger, 2007).

In the present study, we re-examine fluid flow pattern around intrusions in order to delineate the most favorable zones for ore deposition, as defined by a dynamic criterion. Our numerical

simulations (where transient heat and fluid flow equations are coupled) deal only with fluid

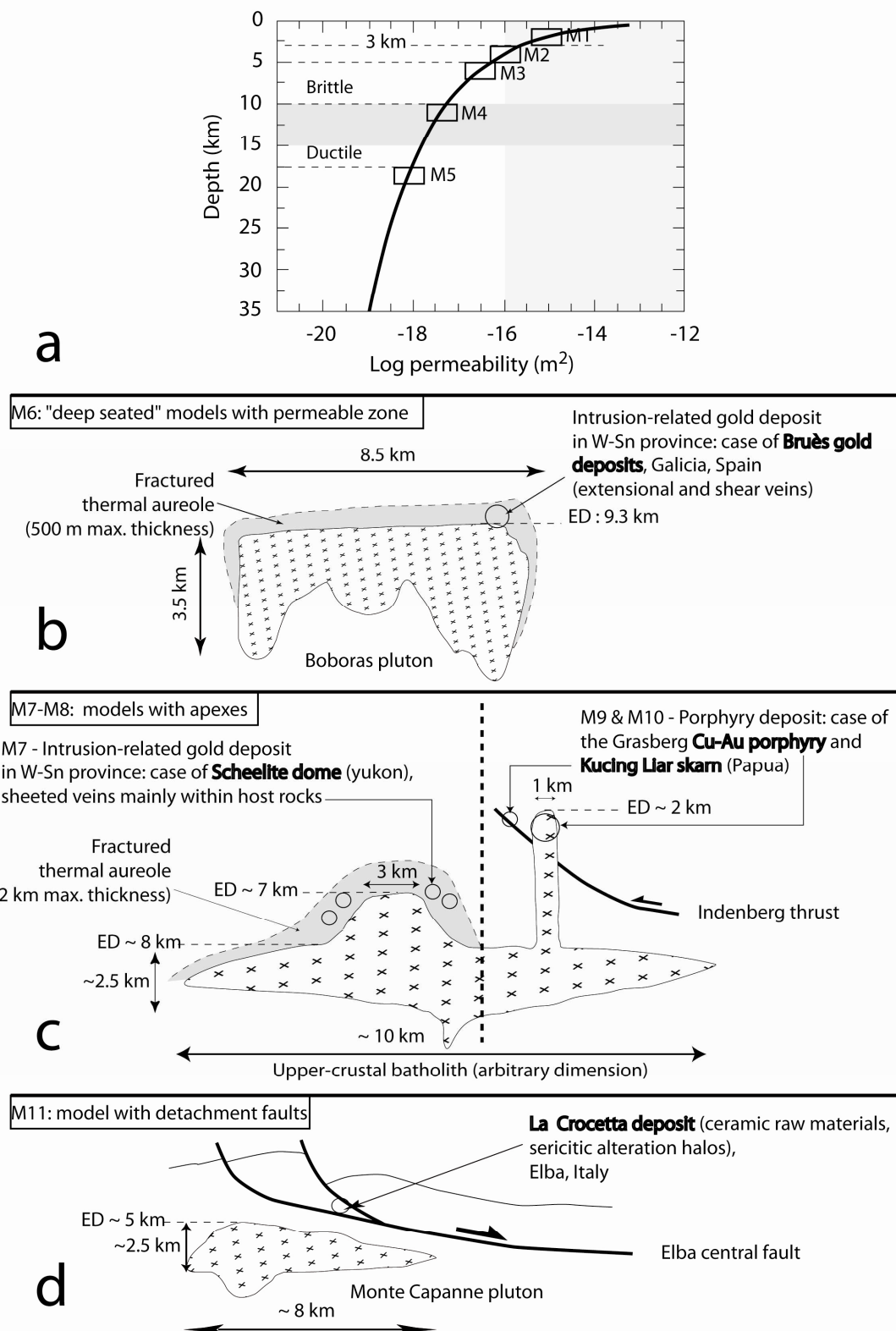


Figure (III.1): Compilation of the geometries, emplacement depth (ED) and geological context for different tested studies (see the text for more details). A: Emplacement depth of models M1-5 along the depth-permeability

curve used in this study (modified from Manning and Ingebritsen, 1999). All intrusions are 10 km width and 2.5 km-thick (see Figure III.2). Permeability threshold of free convection (10^{-16} m^2) established from literature B: Synthetic sketch of the Boboras pluton the associated Bruès gold deposit, Hercynian belt, Galicia, Spain (model M6). C: Natural examples of intrusion-related ore deposits associated with plutonic apexes. ED and dimensions (10 km x 2.5 km) of the main plutonic body (i.e. the upper crustal batholith) are realistic approximations. Models M7-8 is based on the Scheelite dome gold deposit. ED of the stock roof and mineralization (i.e. 7 km) is shallower than M6. M8 present a fractured aureole, absent in M7. Models M9 and M10 represent typical case of a porphyry-type mineralization; the selected example is the famous Grasberg Cu-Au porphyry in the Irian-Jaya fold and thrust belt. Different hypothesis will be tested: M9 without fault, M10 with fault. D: M11, models of fluid flow around plutons emplaced during low-angle extensional faulting. Geometries and structures of the Monte Capanne pluton and La Crocetta raw material deposit along the Elba central detachment.

convection triggered by heat source emplacement (i.e. plutons). Thus, excluding fluid production and solute transport, our models are designed to highlight and test some important points and hypotheses neglected in previous works:

First, fluid flow pattern has been explored below the intrusion, around the floor zone. Within a thermally equilibrated crust, the floor zone is obviously not symmetric to the roof zone through horizontal mirror operation. It is noteworthy that we address magma ascent through the dyke propagation mechanism (Clemens and Mawer, 1992). Hence, thermal structure of crust below the pluton is supposed to be less disturbed than during diapiric ascent mechanism. second, as our models are scaled to simulate large plutons within a 24 km-thick continental crust, the permeability-depth curve of Ingebritsen and Manning (1999) or Manning and Ingebritsen (1999) (figure III.1a) has been applied rather than uniform, layered or stochastic permeability models (Norton and Knight, 1977; Gerdes et al., 1998). Introduction of a depth-dependent permeability model may have important impact on fluid flow patterns. Third, an attempt has been made to evaluate the ore deposition potential. We used an improved version of the concept of Rock Alteration Index (RAI), as defined by Phillips (1991) and used by others (Zhao et al., 1998; Harcouët, 2005), and compared our results to natural well-constrained intrusion-related metal deposits. Gow et al. (2002) also undertook a numerical approach but used uniform permeabilities and investigated steady-state mineralization patterns; fourth, in previous fluid flow models (see references above), the cooling phase only was modeled, without taking into account the emplacement phase (heating phase). Even if this assumption is valid for small shallow intrusions (emplacement less than 100 000 years (Petford et al., 2000), melt production and pluton emplacement may take place over several million years in collision settings with no mantle contribution (Annen et al., 2006).

Moreover, accounting for magma emplacement duration implies that the maximum advective regime is expected to occur during the hottest phase of intrusion, before the cooling phase. Thus, in this study, sequential emplacement and subsequent cooling have been modeled in order to depict fluid flow patterns from incipient pluton inflation stage to the thermal re-equilibration into the crust. Possible effects of the intrusion shape, the emplacement depth and the role of stocks and permeable zones (such as fractures and/or faults) have been evaluated and related to hydrodynamics, duration of hydrothermal system and mineralization potential.

2. Intrusion-related ore deposits: tested natural examples

Several well-constrained natural cases of intrusion-related ore and raw material deposits have been selected in order to depict influence of various factors on the hydrodynamics of such systems. Principal characteristics of these deposits are summarized thereafter and are located in figure (III.1). Boboras pluton (318 ± 5 Myr) and its associated Bruès gold deposit (figure III.1B (M6)) have been selected to test the role of fractured thermal aureole associated with deep seated intrusion (data from Gloaguen et al., 2003; Gloaguen, 2006). It is located within the internal zone of the Spanish Hercynian belt of Galicia. Age of gold mineralization is uncertain (potential regional thermal resetting), but structural controls and fluid inclusions strongly argue for a coeval genetic link between granite emplacement and mineralizing event. Hosting micaschists are strongly veined (partially mineralized) within the thermal aureole.

Fluid expulsion from pluton might have caused hydraulic fracturing within the thermal aureole, which then appears as a high permeability zone. Note that the Bruès gold deposit is located at the roof zone around the northern edge upon a root zone. This gold deposit is characteristic of a deep seated intrusion-related gold deposit in Sn-W Province as defined by Lang and Baker (2001) and Thompson et al. (1999).

Natural examples of intrusion-related ore deposits associated with plutonic apexes have been also tested to depict the potential role of apexes. The Scheelite dome gold deposit (case M7-8, figure III.1c) is a well-established case of intrusion-related gold deposit in a Sn-W Province, around an apical granitic stock and co-genetic with it (Baker and Lang, 2001; Mair et al., 2006; Stephens et al., 2004). As in Boboras pluton, thermal aureole of the apex is intensively fractured and veined. Emplacement age of intrusion and mineralization occurred between 94 and 92 Myr. For a typical case of Porphyry-type mineralization (case M9-10, figure III.1c), we selected the famous Grasberg Cu-Au porphyry in the Irian-Jaya fold and thrust belt (see synthesis in Pollard et al., 2005). Ages span a 3.4–3.0 Myr interval from the first intrusive phase to the last mineralizing event. Along the Indenberg thrust, Kucing Liar Cu-Au skarn (3.4 Myr) is coeval with incipient intrusive phase of the Grasberg complex. For both Scheelite

Dome and Grasberg deposits, realistic size (i.e. 10*2.5km) for the main underlying plutonic body (i.e. the upper crustal “batholith”) have been applied.

As a high permeability zone, detachment fault might have played an important role in channeling mineralizing fluid during extensional regime. Thus, we are interested in exploring fluid flow pattern around plutons emplaced during low-angle extensional faulting. Geometries and structures of the Monte Capanne pluton and La Crocetta deposit along the Elba central detachment is a well-constrained example of such system (case M11, figure III.1D, data compiled from Bouillin et al., 1993; Maineri et al., 2003; Rossetti et al., 2007). La Crocetta is an important economic concentration of ceramic raw materials, resulting from a strong hydrothermal alteration linked to the Monte Capanne magmatic activity. Pluton emplacement and sericitization at La Crocetta occurred between 7 and 6.8 Myr. It is noteworthy that hydrothermalism and mineralization of all tested deposits occurred within a maximum of 2Myr of magma emplacement.

3. Hydrothermal modeling: governing equations and parameters

For a fluid-saturated porous media (rock matrix), the mass conservation equation for variable density fluid without internal fluid source is:

$$\frac{\partial(\phi * \rho)}{\partial t} = -\nabla \cdot (\rho \vec{u}) \quad (\text{III.1})$$

where ϕ is the porosity; ρ is the density of fluid, t is time and \vec{u} the fluid velocity vector (see Table 1 for units). Fluid is assumed to be incompressible with a constant chemical composition, and its density is temperature-dependent. The Darcy’s law was used to describe the fluid velocity field:

$$\vec{u} = \frac{-K}{\mu} (\nabla P + \rho_f \vec{g}) \quad (\text{III.2})$$

Where K is the intrinsic permeability; μ the dynamic fluid viscosity; P the fluid pressure, \vec{g} the gravitational acceleration vector. The permeability has been varied with depth, using the equation of Manning and Ingebritsen (1999):

$$\log(K) = -14 - 3.2 \log(z) \quad (\text{III.3})$$

where Z is depth expressed in km.

The fluid density was considered as a function of temperature only, one gets:

$$\rho = \rho_0 (1 - \alpha_v (T - T_0)) \quad (\text{III.4})$$

Where ρ_0 is the fluid density at room temperature T_0 and α_v the volumetric coefficient of thermal expansion of the fluid.

Based on analytical approximation for the relationship of viscosity with temperature T (Kestin et al., 1978), fluid dynamic viscosity is given by:

$$\mu = 2.414 * 10^{-5} * 10^{\left(\frac{247.8}{T-140}\right)} \quad (\text{III.5})$$

where T is in K and μ in Pa.s. Heat transport is achieved by both conduction and advection in porous media for an incompressible single fluid, and is described by the partial differential equation:

$$Q = C_{eq} \left(\frac{\partial T}{\partial t} \right) + \nabla \left[-\lambda_{eq} \nabla T + C_L \bar{u} \nabla T \right] \quad (\text{III.6})$$

$[-\lambda_{eq} \nabla T + C_L \bar{u} \nabla T]$ represents the total heat flux and is composed of the conductive heat flux (first term) and the advective heat flux (second term). Q is the heat source provided by the pluton. C_L is the volumetric heat capacity $\rho_f C_p$, and C_p is specific heat capacity. C_{eq} and λ_{eq} are weighted average volumetric (or "equivalent") heat capacity and thermal conductivity respectively, as defined in saturated porous media:

$$C_{eq} = \left(\frac{\left(\sum \phi_f \rho_f C_{p_f} + \sum \phi_s \rho_s C_{p_s} \right)}{\left(\sum \phi_f + \sum \phi_s \right)} \right) \quad (\text{III.7})$$

where f and s subscripts for fluid and solids embeddings). The equivalent thermal conductivity writes:

$$\lambda_{eq} = \left(\frac{\left(\sum \phi_f \lambda_f + \sum \phi_s \lambda_s \right)}{\left(\sum \phi_f + \sum \phi_s \right)} \right) \quad (\text{III.8})$$

Where λ_f and λ_s are thermal conductivities of the fluid and the country rock.

Fluid flow and heat transport are coupled through the density and viscosity of fluids (equations 4 and 5).

4. Defining a Restricted Rock Alteration Index

Coupling of heat and fluid flow equations has been computed numerically, with temperature-dependent properties (i.e. density, viscosity, heat capacity and thermal conductivity) and depth-dependent permeability. In order to gain some insight into how mineralization patterns can be deduced from thermal and velocity field, one may start from the initial work of Phillips (1991), who derived a mineralization rate which depends on diffusive and advective

processes. In short, fluids carrying dissolved chemical species move through a permeable matrix or fractures network. The resulting patterns of dissolution, precipitation, and fabric alteration depend on the reaction kinetics and on the influence of temperature, pressure and other constituents. However, in many geological situations, the controlling factor is the rate at which reactants in solution can be delivered to the reaction site by advection and diffusion in the flow. The dissolution/precipitation of an aqueous mineral is mainly dependent on advection term since diffusive processes are negligible when large-scale processes (fluid circulation over a large timescale) are considered.

As in buoyancy driven convective flows, the fluid pressure gradient is small, the sign of the mineral dissolution/precipitation rate depends on the scalar product of fluid velocity vector by temperature gradient (for more details see Phillips; 1991; Zhao et al. 1998; Raffensperger and Vlassopoulos, 1999; Zhao et al., 2001; 2003; Harcouët 2005). This scalar is called the Rock Alteration Index, or RAI, and is defined as:

$$RAI = \bar{u} \cdot \bar{\nabla} T \quad (III.9)$$

With an additional hypothesis on the sign of the partial derivative of solute concentration with taking into account the temperature, Phillips (1991) deduced that if RAI is positive, then mineral dissolution occurs, whereas for a negative value of RAI, mineral precipitation is promoted. Since RAI unit is expressed as $K \cdot s^{-1}$, one may interpret negative RAI values as local cooling rates of the fluid, while positive values would correspond to local heating rates.

During regional metamorphism, pluton acts as second order intense fluid flow perturbation within slower regional fluid flow (Stern et al, 1992). For active regional metamorphism, a Darcy velocity of $10^{-11} \text{ m} \cdot \text{s}^{-1}$ is considered to be an average value (Ingebritsen and Manning 1999). For contact metamorphism, Darcy velocities, from time integrated flux based on mineral reactions and stable isotopes studies range from $10^{-9} \text{ m} \cdot \text{s}^{-1}$ to $10^{-11} \text{ m} \cdot \text{s}^{-1}$ (Ferry et al., 2002). Hydrothermal numerical models of contact or regional metamorphism, predict Darcy velocities ranging from $10^{-8} \text{ m} \cdot \text{s}^{-1}$ to $10^{-11} \text{ m} \cdot \text{s}^{-1}$ (Cook et al., 1997; Gerdes et al. 1998; Oliver et al. 2006). Thus, in order to decipher the pluton contribution to fluid flow, a restricted fluid velocity condition ($u > 10^{-10} \text{ m} \cdot \text{s}^{-1}$) was added parallel to RAI. This restricted RAI (R^2AI) is defined by the logical expression:

$$R^2AI = [RAI < 0 \text{ and } u > 10^{-10} \text{ m} \cdot \text{s}^{-1}] = 1 \text{ If it is valid and } 0 \text{ if not} \quad (III.10)$$

5. Model construction: geometry, timing, boundary conditions and rock properties

5.1 Geometry

We constructed our models based on theoretical and selected well-known natural cases (M1 to M11, figure III.2). Along the depth-permeability curve of Manning and Ingebritsen (1999),

the models (M1 to M5) were performed to study the effect of emplacement depth on hydrothermal circulations and being as references for natural cases (figures III.1, 2). The basic geometry chosen for theoretical models (M1 to M5) was a rectangle with 2.5 km thick and 10 km width with emplacement depth varying from 3 to 17.5 km (figure III.1, 2).

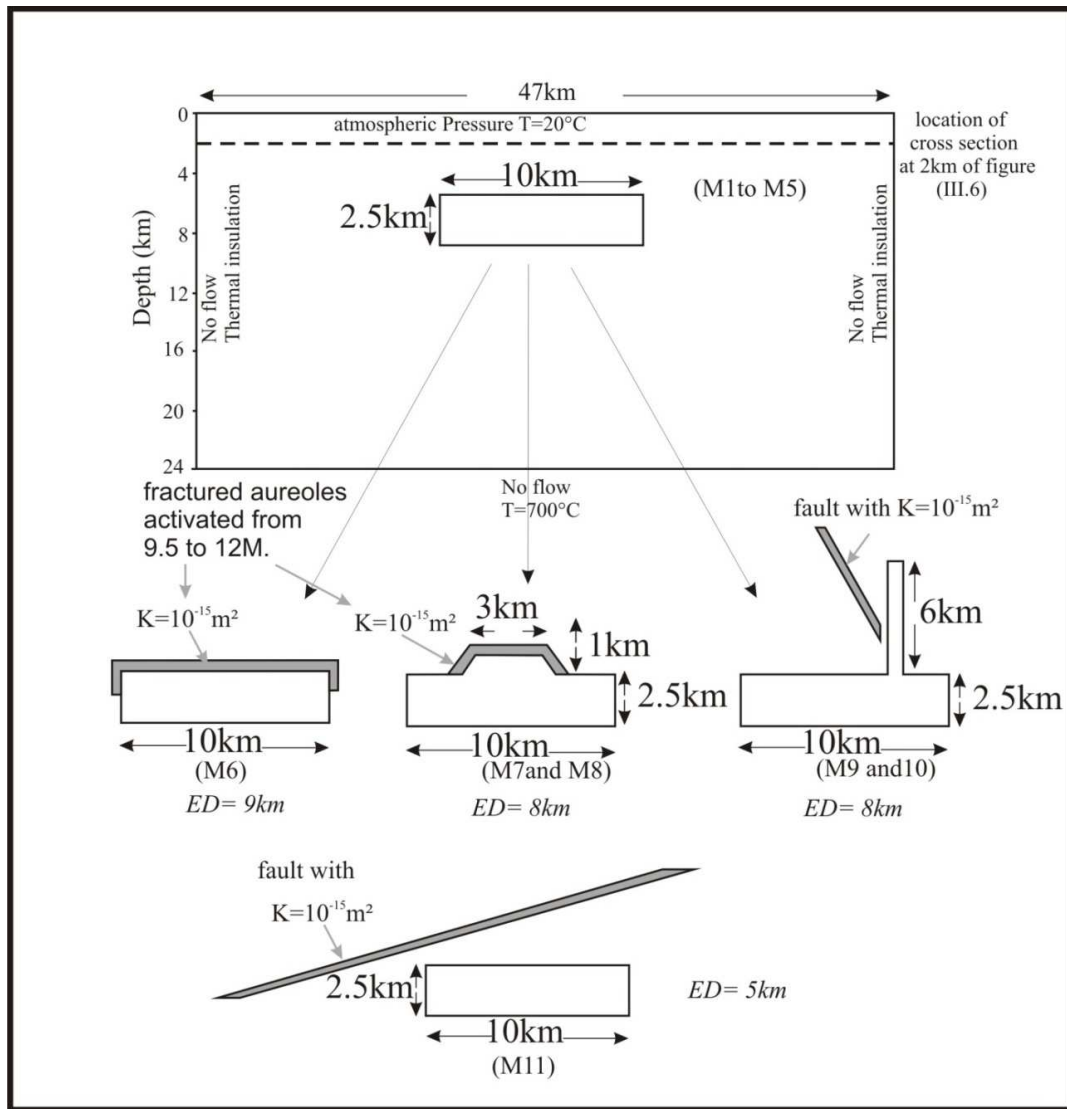


Figure (III.2): Simplified forms and boundary conditions for different models; M1 to M5 represent theoretical models with different emplacement depths while M6 to M11 represent models of tested natural cases, ED: emplacement depth of the intrusion roof. See text for more details.

In addition, models (M6 to M11 in figure III.2) were constructed to adapt the natural examples (figures III.1b, c, and d). The pluton area ranges from 25 to 31 km² and the roof of pluton covers depths ranges from 8 to 10 km. For the continental crust, we have used 2D model geometry of 47 km in width and 24 km in depth (figure III.2). Geometries of plutonic apexes, fractured aureoles and surrounding faults are described in figure (III.2).

5.2 Timing

Our transient models were designed to take into account the time of emplacement (cf. introduction). Total duration of numerical experiments is 20 Myr. From 0 to 7 Myr., the initial imposed (a priori) thermal state evolves by adjusting thermal field to the effective boundary conditions and material properties, until a steady-state is achieved. Duration of emplacement, represented by a time-varying heat source, lasts 3 Myr. (from 7 to 10 Myr).

The maximum temperature (the hottest phase) at the intrusion centre occurs therefore at 10 Myrs. The subsequent cooling phase occurs from 10 to 20 Myr, after which thermal equilibrium is reached again.

5.3 Boundary conditions and rock properties

The upper boundary represents the flat surface topography, which is permeable and maintained at 293K (T_0). The bottom is located at 24km depth with temperature fixed at 973K. The lateral boundaries are assumed to be impermeable and thermally insulated.

The initial thermal gradient inserted in the model is:

$$T = 293 + (0.024 \cdot Z) \quad (\text{III.11})$$

For simplification, the host rock was assumed to be a homogeneous saturated porous medium (constant porosity = 0.5%) with a depth-dependent permeability (Eq. III.3).

The intrusion has physical characteristics of granite and its centre reaches 973K (700°C) at the hottest phase. As magma above 400°C is considered as impermeable body, we fixed the permeability of intruded body at 10^{-24}m^2 during the emplacement from 7 to 10 Myr. This very low permeability implies no fluid production by the pluton. Before and after emplacement, the pluton permeability follows the depth-permeability curve (Eq. III.3).

High permeability zones such as faults (figures III.1, 2) have been modeled with constant permeability (K value of 10^{-15}m^2), whereas, fractured aureoles around pluton are transient permeable zones, which has been activated (K value of 10^{-15}m^2) from 9.5 to 12 Myr. Before and after this time span, the permeability of the aureole zone follows the depth-permeability curve (Eq. III.3). Our 2D models include one single homogenous fluid phase (pure water) which was chosen in order to compare with published models.

Finally, the coupled models have been performed using a commercial finite element code (Comsol Multiphysics™) which has been tested with various other configurations already published before (see benchmark in next section).

6. Fluid flow patterns: results and discussion

6.1 Benchmark

To validate our model, we simulated several cases explored by published models (Rabinowicz

et al., 1998; Gerdes et al., 1998). The example shown in figure 3 comes from Gerdes et al. (1998) where they solve transient hydrothermal circulation during pluton cooling. We reproduced their work after fitting the most probable bottom thermal boundary condition; the results of this model match those from the published study (figure III.3). We also reproduced results obtained by Rabinowicz et al. (1998), where higher permeabilities were involved. Identical unsteady convective patterns and steady-state ones were obtained within a rectangular box with permeability 10^{-15} m^2 and $5 \cdot 10^{-15} \text{ m}^2$, respectively. In addition, for these two last cases, surface heat flow values and variations were recovered.

6.2 Spatial-temporal evolution of the fluid flow pattern and heat transfer

Even when streamlines described convective cell in different models before the emplacement (see below), heat transfer by advection may be neglected since fluid velocities are low (lower than $10^{-14} \text{ m.s}^{-1}$).

To estimate the efficiency of thermal advection, we used a local Peclet number (Pe) which denotes the ratio between advection and thermal diffusion. When the Peclet number is low (<1), the influence of heat advection is weak because of the slow fluid velocity. The critical Peclet number above which the influence of heat advection becomes significant is (>1).

During the cooling phase (after 10Myr), within the pluton roof area, fluid flow patterns obtained in this study correspond to those observed in previous studies (e.g. Norton and Knight 1977; Driesner and Geiger, 2007): fluids inside the host rock migrate toward the upper corners of pluton and create two convection cells above the pluton. The cell in the left side is anticlockwise, while the cell in the right side is clockwise. The pluton floor zone is characterized by a convergent fluid flow from both deep and shallow zones.

During cooling phase of shallow plutons, shallow fluids may migrate beneath the pluton. This constitutes a typical cooling fluid flow pattern. For shallow intrusions (such as model M1 (figure III.4), where the pluton is emplaced in a permeable zone of host rock), streamlines and isotherms are disturbed by a second order convective instability above the pluton roof (M1 and M2 in figures III.4 and III.5 respectively).

This is well expressed in figure (III.6), where the horizontal component of the fluid velocity is shifted from positive to negative value through four convective half cells. These second order convective cells depend on pluton length and emplacement depth, and may be important when considering mineralization potential.

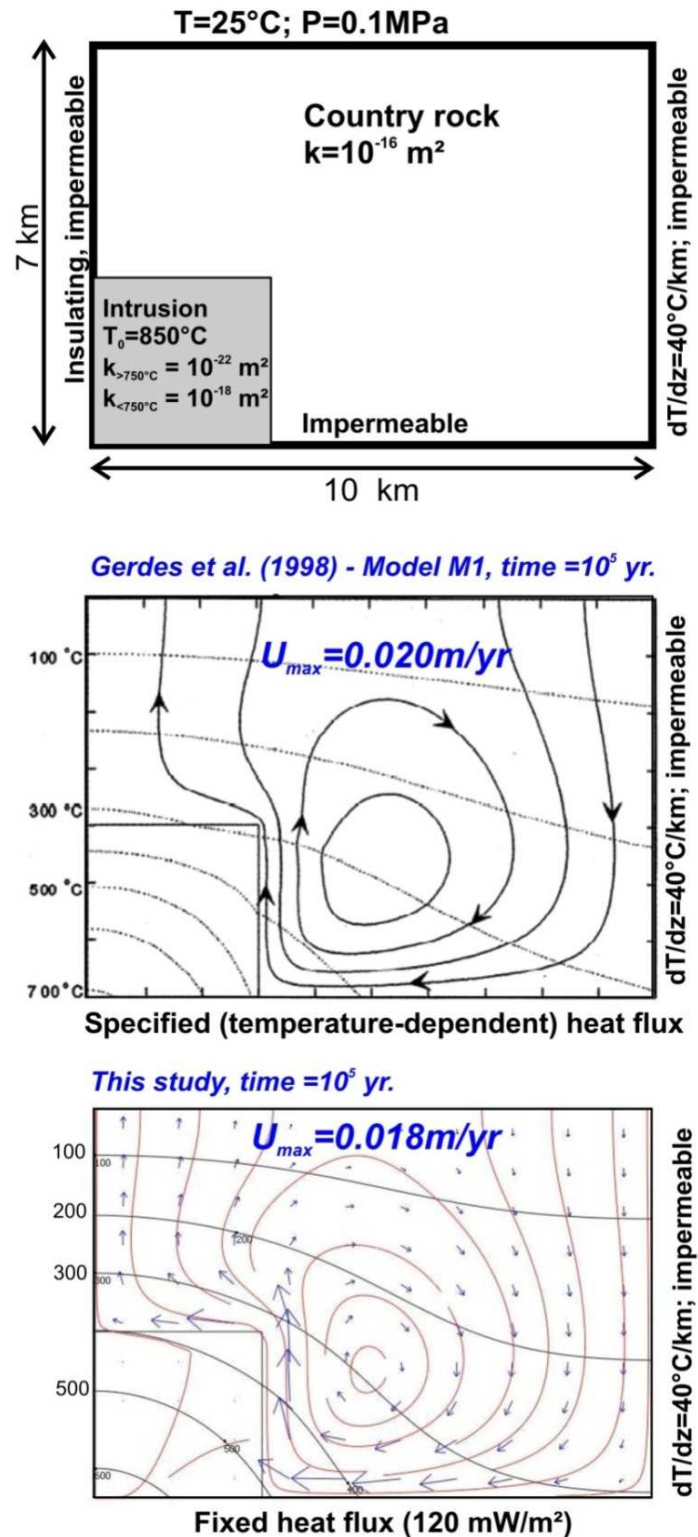


Figure (III.3): Benchmark test of our hydrothermal modeling. Model M1 of Gerdes et al., (1998) at 10^5 years is shown on the middle. Our model at the bottom reproduces at the same time the same thermal and fluid velocity patterns with a fixed heat flux condition at the base.

For shallow plutons, mapping of Pe number indicates that advective heat dissipation is still dominant 10^5 years after the hottest phase.

The main convective discharge zone appears to be the area above plutons and represents the most advective zone (M1 to M3, figures III.4, 5 and 7). As additional convective cells in M1 create two discharge zones (rather than one single for M2 and M3, figure III.4), the advective zone geometry presents two advective apexes for the chosen pluton length.

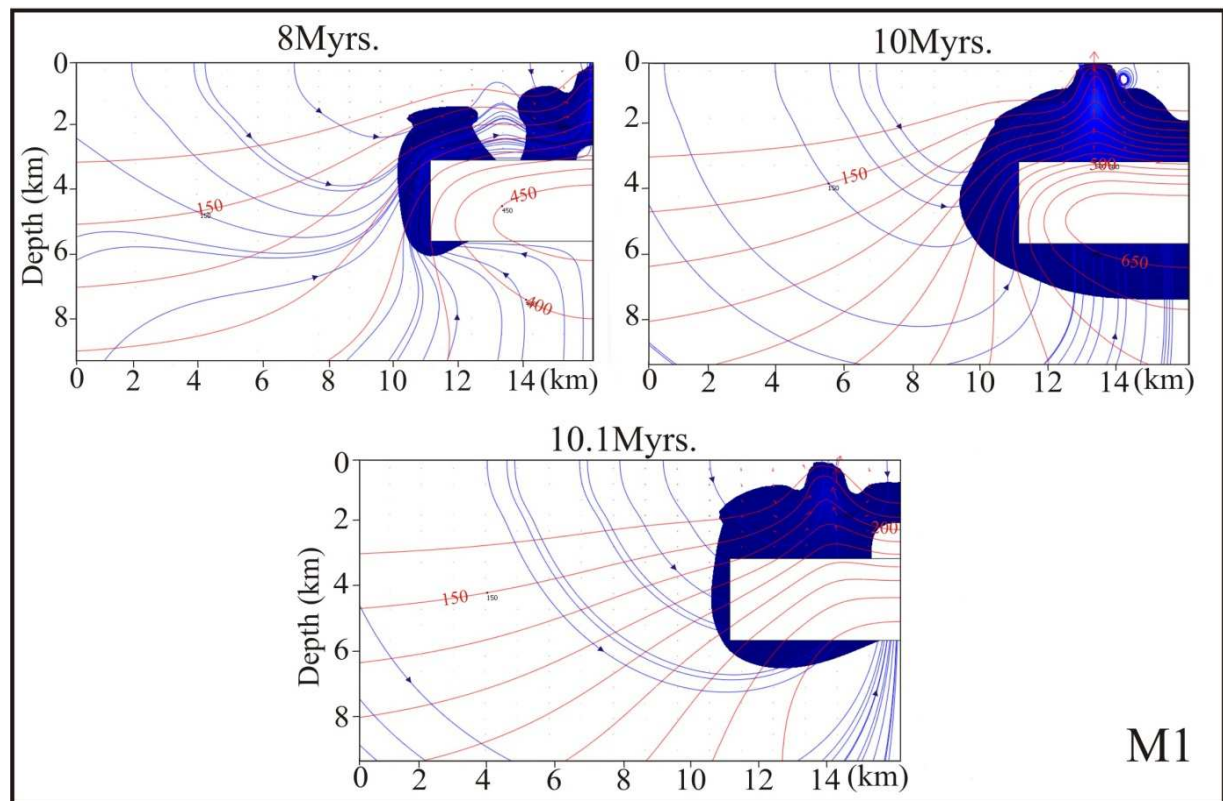


Figure (III.4) Snapshots of different time steps of M1, The blue area represents the advective zones ($Pe > 1$) around pluton ($Pe=1$ in blue and increases in values to 6 (from blue to red for other models)). Streamlines are in blue and labeled isotherms in red. Red arrows represent fluid velocity vectors.

Moreover, as our models are designed to simulate long-lived magma injection, fluid flow and thermal transfer during magma emplacement can be investigated. Firstly, as expected, for all emplacement depth, extent of advective zones is the maximum at the hottest phase of melt injection (i.e. 10 Myr). This constitutes an important difference with models testing only cooling phase of plutons (e.g. Norton and Knight, 1977).

Secondly, shallow hydrothermal systems as M1 reach a cooling flow pattern (i.e. regular and concentric streamlines) before the hottest phase of emplacement. Before the establishment of this cooling flow pattern, divergent buoyant fluids that are expelled downward and laterally from the pluton roof zone are responsible for the deflection of streamlines beneath the pluton. This deflection of streamlines is characteristic of a warming flow pattern resulting in bell shape in M3 and M4 (figure III.7 & 8, time 10 Myr).

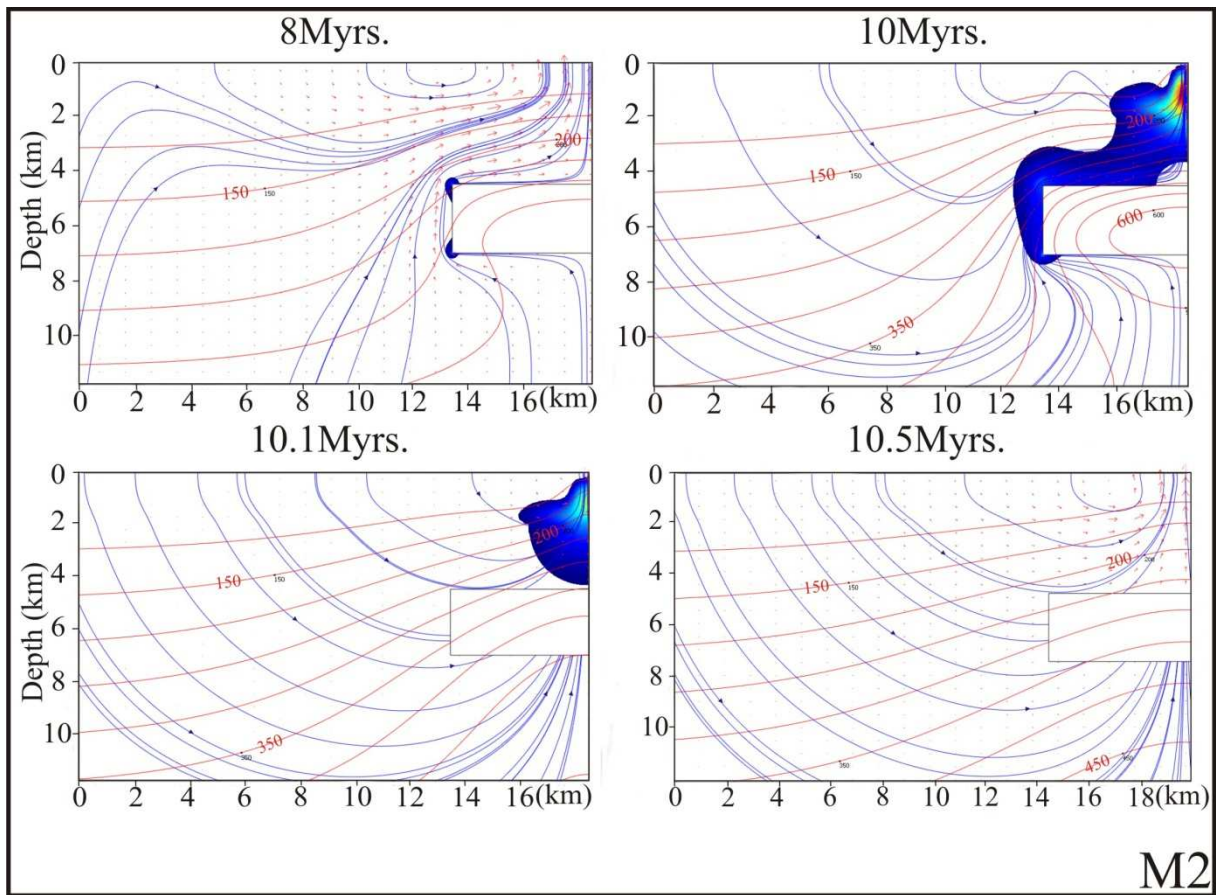


Figure (III.5) snapshots of different time steps of M2 model, velocity streamlines represented by blue line while thermal contours represented by red lines.

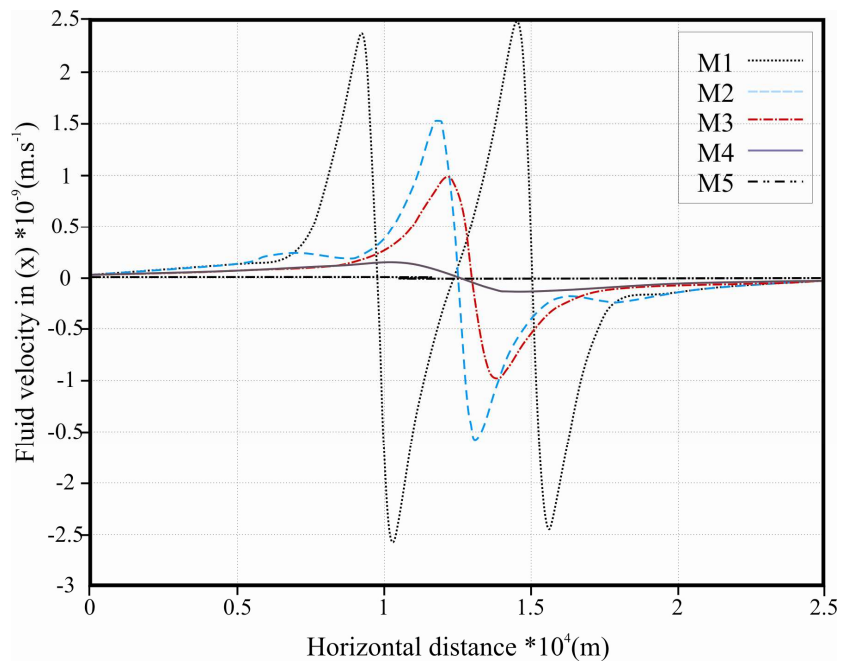


Figure (III.6): Horizontal component of the fluid velocity along horizontal cross-sections above the intrusion at the hottest phase of intrusion (i.e. 10 Myr, see cross-section location on figure 2). Each bulge and depression of

fluid velocities in x direction represents a convective cell. The shallowest pluton (M1) shows four convective cells while no significant variation was noted for the deepest pluton M5.

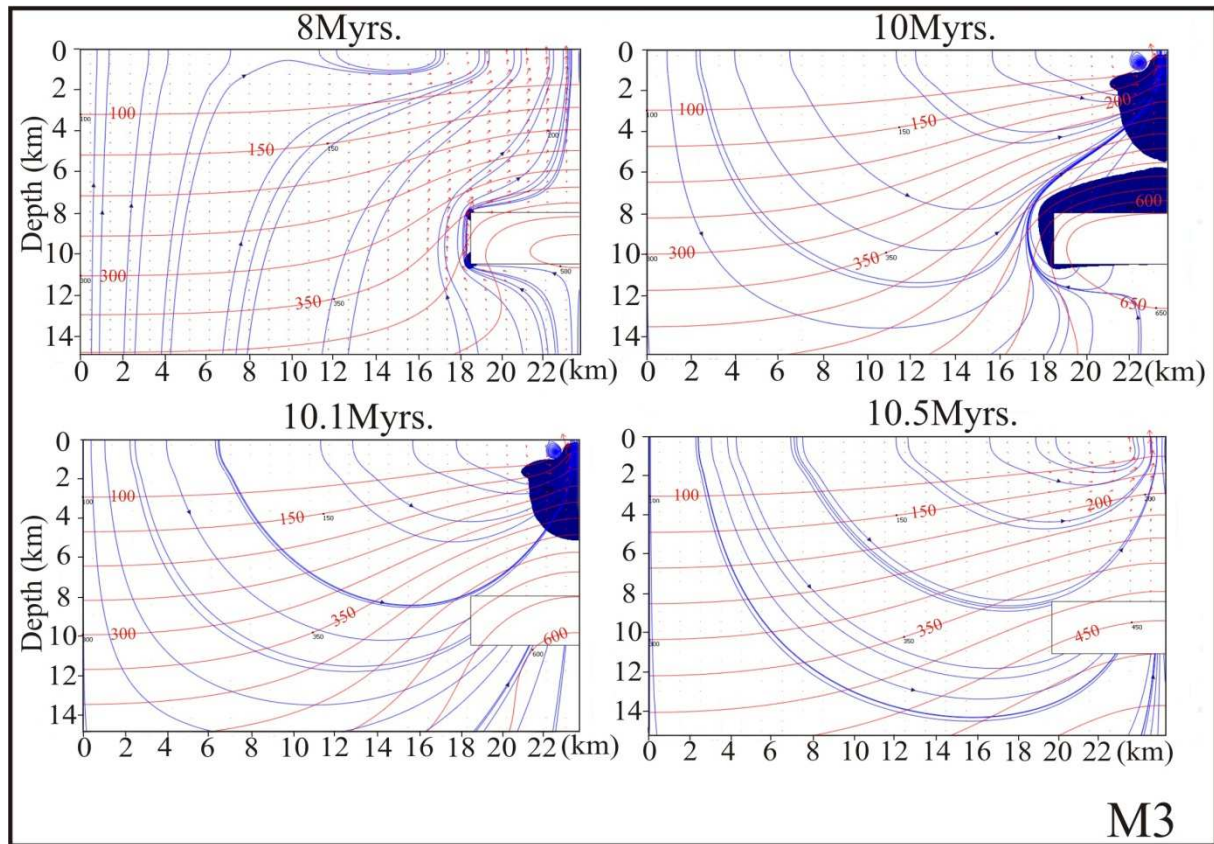


Figure (III.7) Hydrodynamics and illustration of local Peclet number values in different models at different time periods.

6.3 Influence of emplacement depth

For shallow intrusions (model M1, where the pluton is emplaced in permeable zone), four convective cells are distinguished, whereas with M5 (very deep emplacement) no convective cells are present (figure III.9). Significant differences in fluid velocity were identified: with shallow plutons (M1, M2), fluid velocity increased by two orders of magnitude during pluton emplacement (10^{-10} to 10^{-8} and 10^{-11} to 10^{-9} m.s $^{-1}$ respectively), while with intermediate plutons, it increased by only one order of magnitude (10^{-11} to 10^{-10} m.s $^{-1}$). As we considered that fluid velocities lower than 10^{-10} m.s $^{-1}$ were not induced by magma emplacement (cf. above), no significant variation in fluid velocity was noted with deep seated intrusion (M5) (10^{-13} to 10^{-12} m.s $^{-1}$). Peclet number distribution (figure III.4) shows that advective heat transfer decreases with emplacement depth. That is coherent with the removal of convective cells and low fluid velocities with increasing emplacement depth.

All these features are clearly related to the variation of permeability of host rock which is depth-dependent in our models (cf. Equation 3). It is noteworthy that as emplacement depth increases (M1 to M4 in figure III.4) advective heat transfer is restricted around the pluton. From 4.5 to 10 km of emplacement depth (M2 to M4 in figure III.4), at the hottest phase of pluton emplacement, the advective zone at the pluton floor zone thickens. Indeed, at that time, shallow plutons (emplaced in cool embeddings) already present a cooling fluid flow pattern (M1 in figure III.4), whereas deep seated intrusions still present a warming fluid flow pattern (bell shape of M3 and M4 in figure III.4). As a result, for magma emplacement deeper than 10 km depth, pluton buoyant fluids are divergent, and especially downward at the pluton roof zone, may constitute a narrow advective aureole around the pluton. Nevertheless; permeability being low, fluid velocity at the pluton floor zone remains moderate, and cooling is almost achieved by conduction.

6.4 Effects of apexes

To study the effects of added plutonic apexes, models M3, M7 and M9 with the same emplacement depth (8 km) were compared during the intrusion emplacement (figure III.7). In M7 where the apex is located in the deep zone of host rock (where the permeability of host rock is lower than 10^{-16}m^2), no significant role of apex was observed (figure III.10). In contrast, the appearance of apex into the shallow zone (where the permeability is high, M9) disturbs the movement of fluid around main intrusive body by relocating convective cells and discharge zones along the apex rather than around the main intruded body (figure III.11). In the single case (with no apex, M3), fluids circulate upward from the pluton centre. Adding an apex to that geometry makes fluids circulate upward bordering the pluton roof and along the apex. Mapping of local Peclet number values (figure III.11) demonstrates that apices are able to focus the advective zone around them, whereas the advective zone is located mainly around the intrusion in case of single intrusion M3.

As we have considered the magma itself as an impermeable zone, fluids rise and accumulate at the highest point of magma body (which is often stock); we related that to the variation of permeability that is higher in shallow zones (nearby the highest point of magma morphology). As apices reach to shallow zones, effective advection initiates along them during the magma emplacement and before the hottest phase (e.g. M9 at 8 Myr in figure III.11).

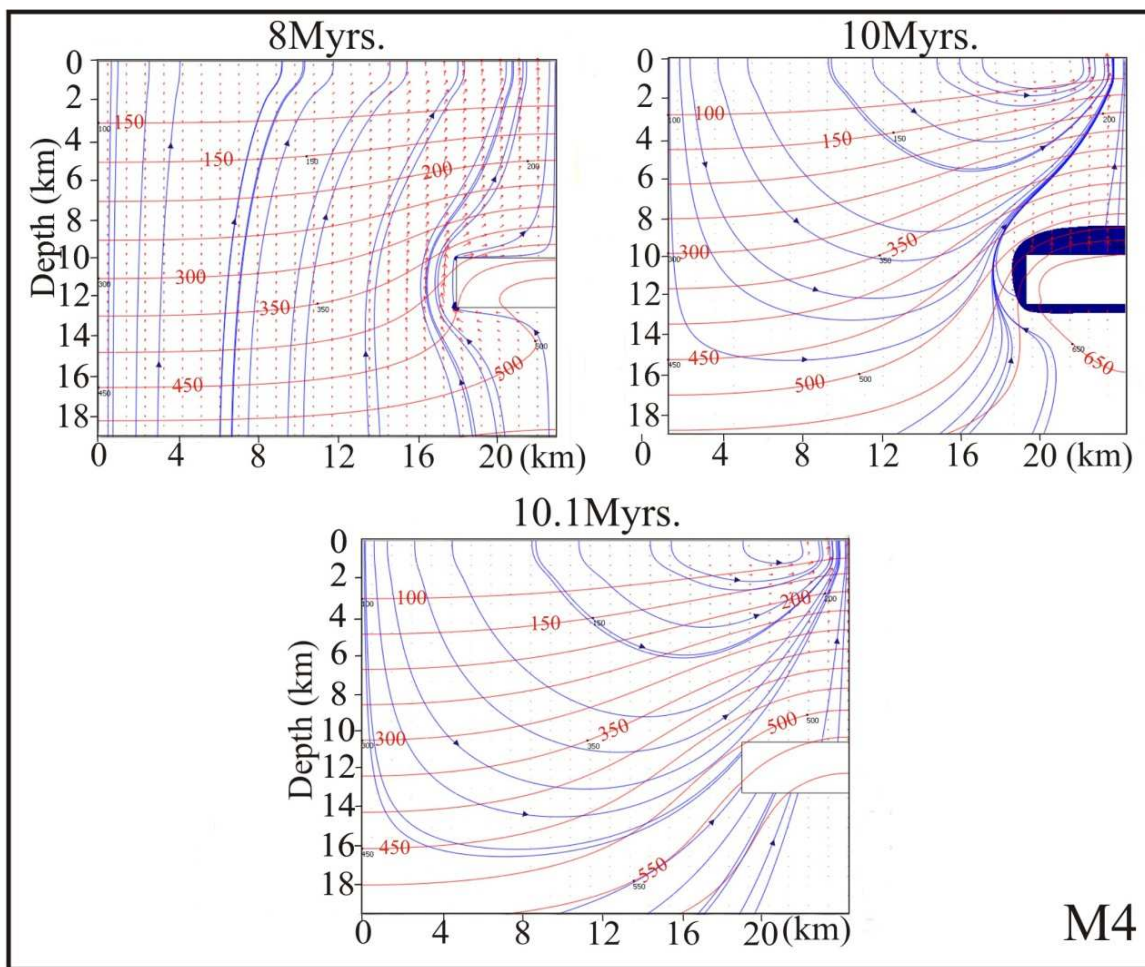


Figure (III.8) snapshots of different time steps for M4.

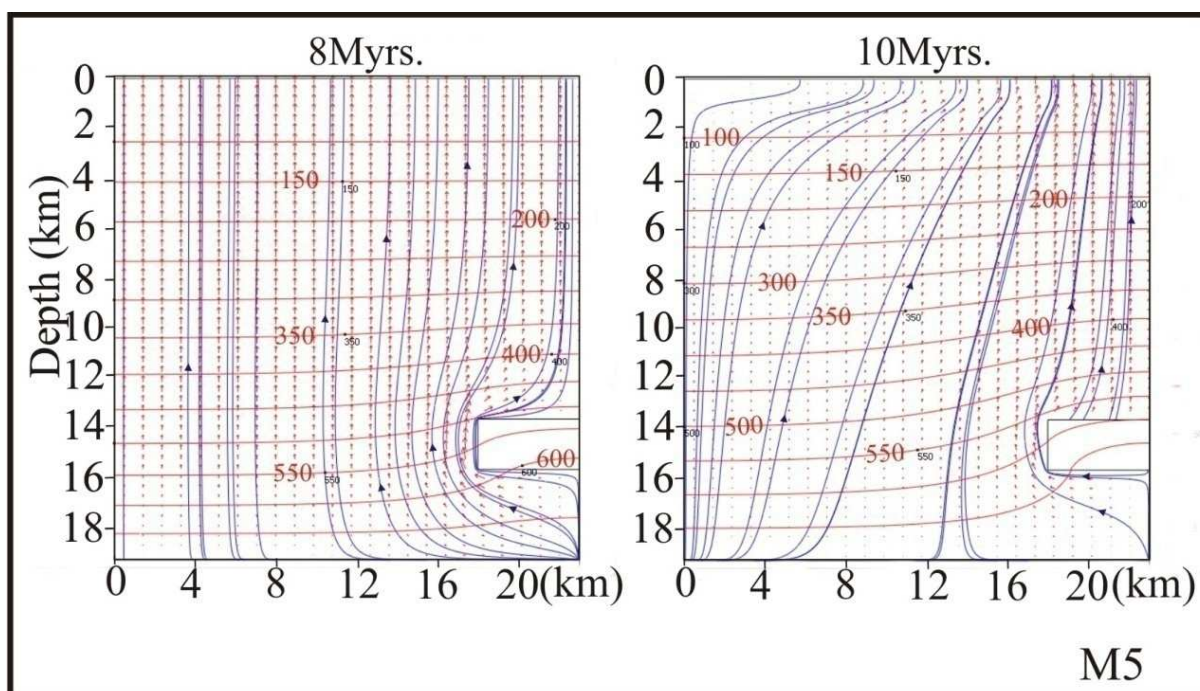


Figure (III.9) snapshots of different time steps for M5.

7. Probable mineralization patterns

The application of R^2AI (Eq. 10) shows probable zones of mineralization for the studied cases of well-known ore deposits (M6, M8, M10, M11). For each case, we depict the evolution of the mineralization potential from the incipient magma emplacement to the cooling phase (figures 7 and 8). To study the effects of fractured aureole and faults, R^2AI in model outputs (M1 to M4 and M7) at the hottest phase of magma emplacement is shown in figure III.12.

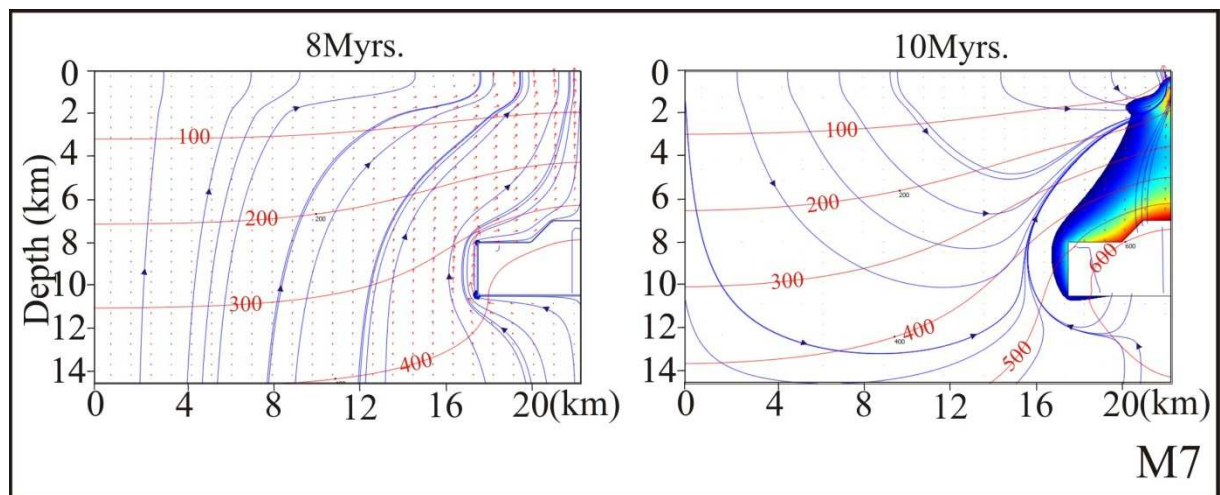


Figure (III.10) snapshots to study the effects of an apex. With deep intrusion, no significant role of apex was noted.

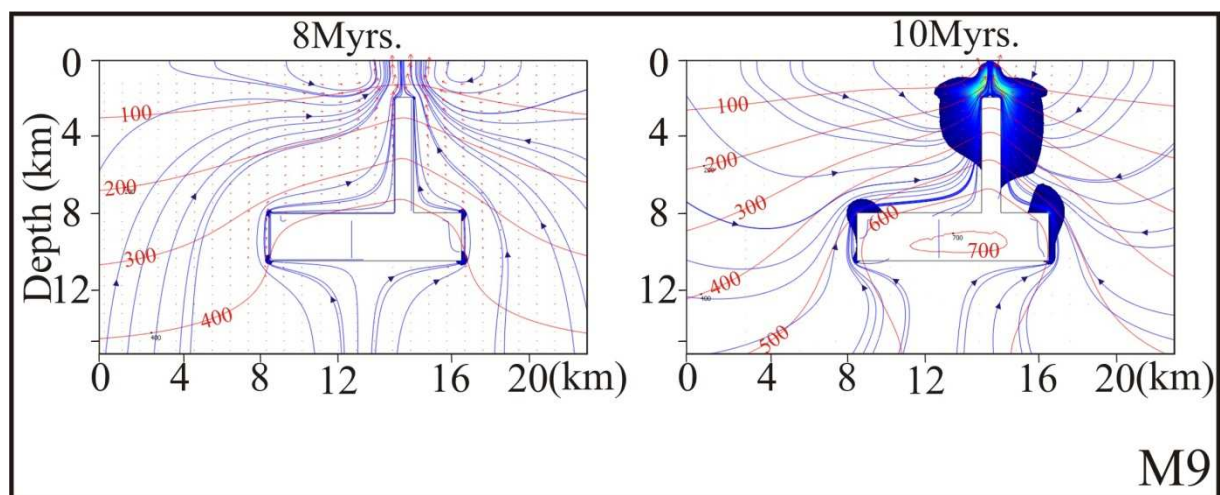


Figure (III.11) snapshots show the effects of an apex. In shallow intrusions, the significant role of apex was noted by shifting the advected zone to be located around apex.

7.1 Potential mineralization zones for models outputs

Comparing with Peclet number and streamlines distributions (figures III.4, 5 &7), favorable R^2AI was found around and above the pluton during the hottest phase (figure III.12) for all studied cases.

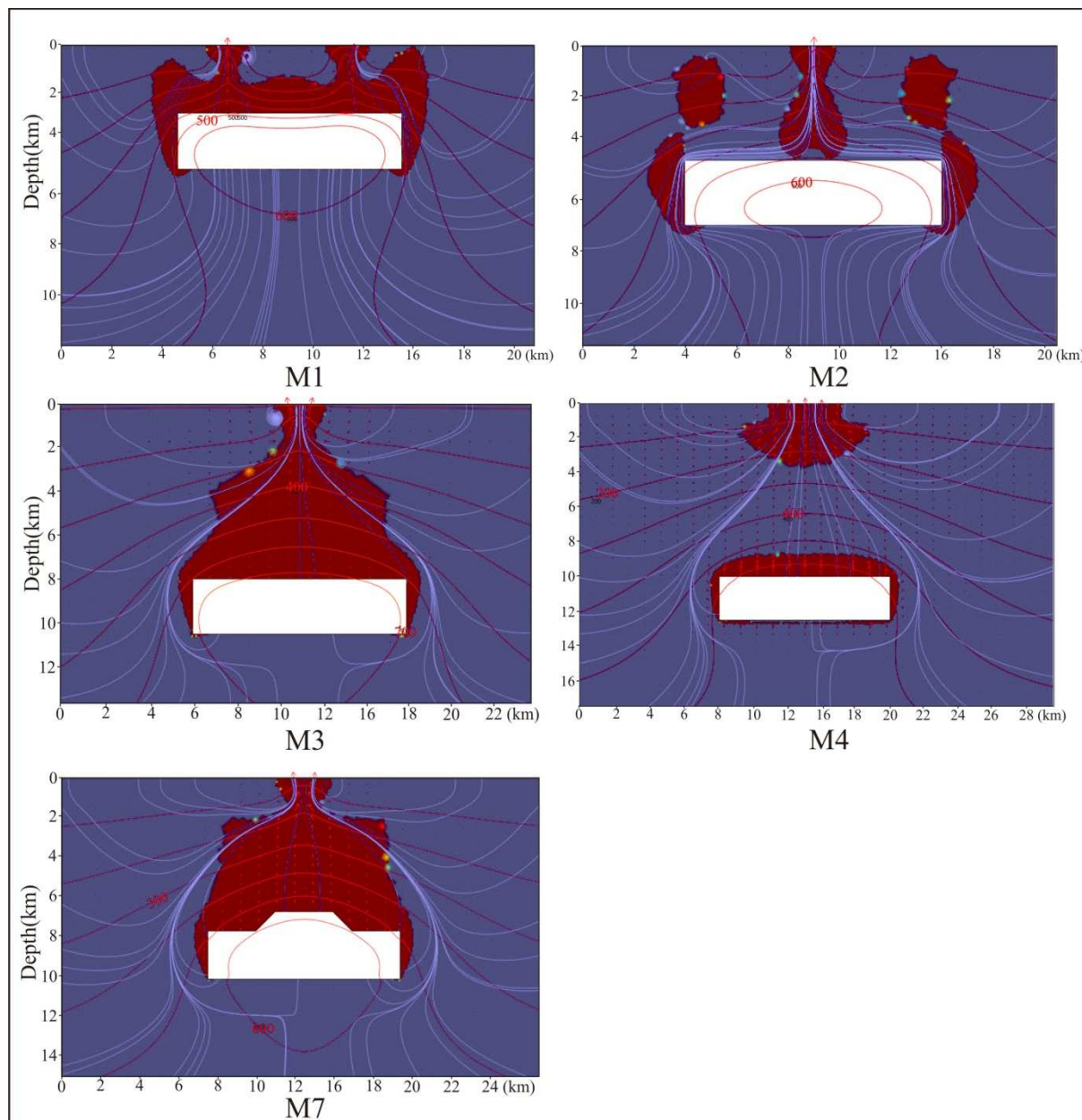


Figure (III.12): R^2AI application around each pluton at the hottest phase (i.e. 10 Myr). Red areas represent physical favorable zone of mineral deposition corresponding to $R^2AI=1$. Streamline in light blue lines and isotherms contours represented here in red lines.

For all tested emplacement depths, no significant favorable mineral deposition area is observed below the pluton floor. Run M1 and M2 presents high potential mineralization zones which are localized along narrow discharge zones near the topographic surface.

They result from second order convection cells that developed above shallow plutons (cf. above). In figures III.4 & 5, these advective narrow zones produce thermal bulges where fluids reach the surface at temperatures ranging from 150 to 100°C. We suggest that these shallow, focused mineralizing zones may correspond to low temperature hydrothermal systems. They may be responsible for either F-Ba (\pm Pb, Zn) mineralization characteristic of late orogenic granite emplacement, or strong alteration leading to kaolinite deposits. The R^2AI distributions are different between M3-M7 and M4, because the permeability of the host rocks overlying the pluton roof in M4 prevents fluids to circulate faster than $10^{-10}m.s^{-1}$. Consequently, the continuous potential zone from pluton roof to the topographic surface in M3 becomes restricted to two separate zones (near topographic surface and around pluton) in M4. For those deep seated pluton, the shallow and the large potential deposition zones in M3 appear unrealistic at first glance. This point will be discussed later.

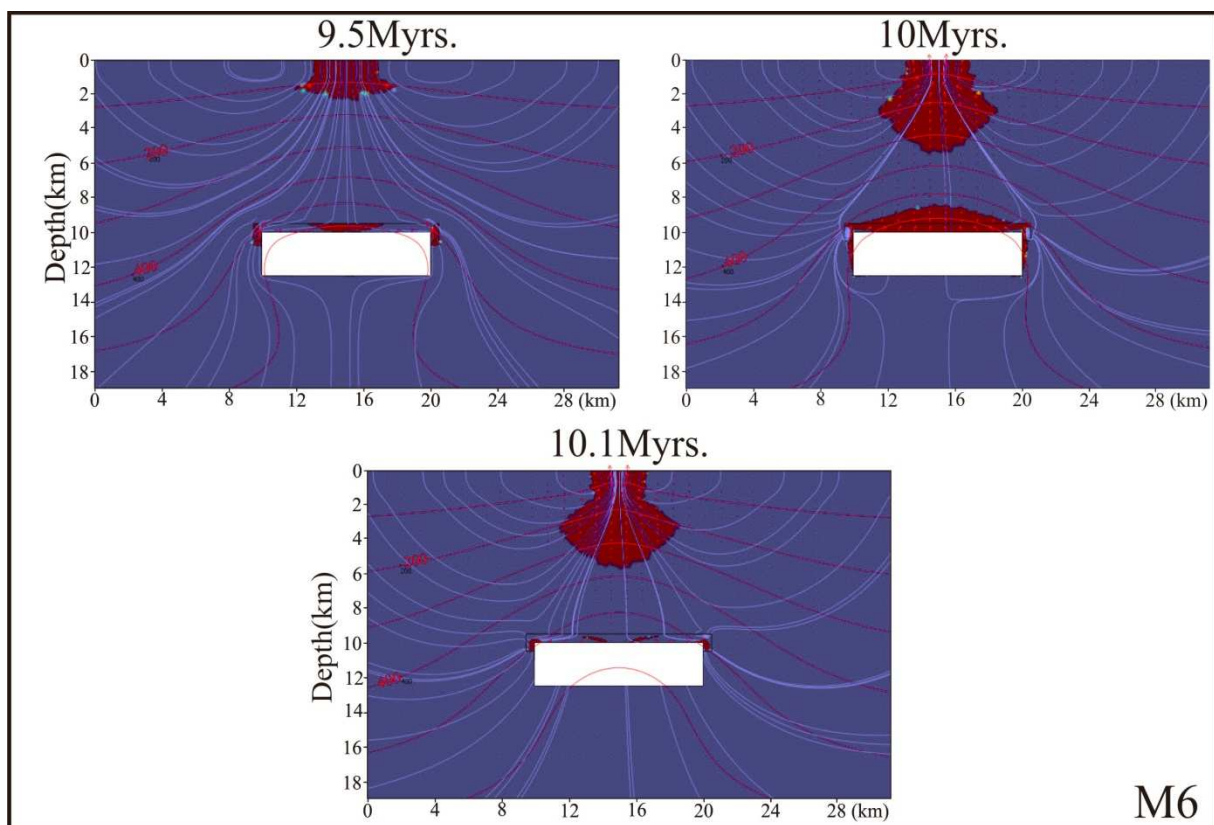
7.2 Effects of permeable fractured aureoles

The model M6, based on the Bruès intrusion-related gold deposit, is emplaced at 9.3 km, i.e intermediate between M3 and M4. The model M8 is based on the Scheelite dome intrusion-related gold deposit and has to be compared to M7. The most important difference between M6 & M8 and theoretical models is the occurrence of fractured thermal aureole that acts as a high permeability zone. These high permeable zones ($10-15m^2$) have been activated late during magma emplacement, at 9.5 Myr, i.e. $5 \cdot 10^5$ years before the hottest phase. The models show that highly permeable fractured aureoles play a key role in the mineralization pattern. Indeed, they are able to pump and focus the fluid flow and therefore to restrain and decrease the extent of favourable zones (figure III.13). In M6 model, upper corners of pluton become the most probable mineralization sites, particularly at 10^5 years of cooling phase. This is in agreement with the location of the Bruès gold deposit at the upper north corner of the Boboras pluton (figure III.1b). Focus and pumping of fluid into permeable zone is also responsible for the good agreement between the Scheelite dome gold deposit and the model M8 (figures III.1c and 13). As suggested before with emplacement depth (8 km), the stock does not play an important role for the R^2AI distribution because the permeability of host rock is still lower than the $10^{-16}m^2$ threshold (M3 vs. M7 on figure III.12).

However, development of a cracked thermal aureole around the stock induced formation of restricted and narrow probable mineralization zone along the stock flanks (M8 figure III.13).

7.3 Effects of apexes

A long apex reaching to shallow zone where permeability is greater than $10^{-16}m^2$ creates a dramatic change in R^2AI distribution (M10, figure III.14). The apex re-localizes the positive R^2AI around it (compare M3 figure III.12 and M10 figure III.14). As expected, the top of the apex acts as small shallow intrusion and plays a role in localizing a probable zone of mineralization, before the hottest phase of the magmatic system. One important implication is that the mineralization potential of main upper-crustal batholith is reduced when the apex is absent (M3, figure III.12). Comparison with natural porphyries (e.g. Grasberg Cu-Au porphyry, figure III.1c) is quite delicate because ore is hosted within the magmatic apex. However, the well-established concentric zoning of alterations halos (i.e. potassic, phyllitic and propylitic, Lowell and Guilbert, 1970) within Cu-porphyry host rocks might correspond to positive R^2AI distribution shown in M10 (figure III.14).



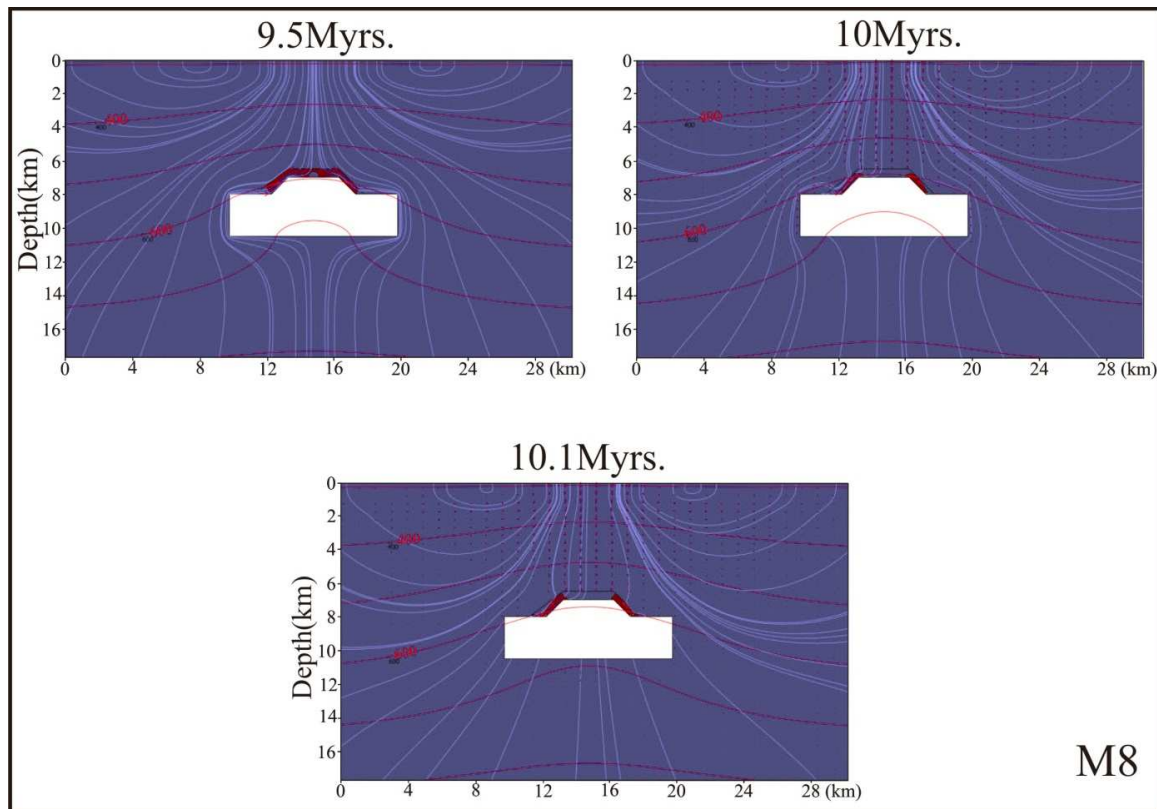


Figure (III.13): Focused snapshots during the warming and the cooling phase of pluton (hottest phase at 10 Myr) associated with fractured thermal aureole and apex. M6 and M8 are simplified numerical models of the Bruès and Scheelite Dome granite-related gold deposits respectively (see figure 1 for geologic context). Red areas are the favorable zones of mineral deposition corresponding to $R^2AI=1$. Streamline represented in light blue lines and isotherms contours in red lines.

7.4 Effects of faults

In our models, faults are activated ($k = 10^{-15} \text{ m}^2$) during the entire duration of the experiment (i.e. 20 Myr). As a result, it is expected that the deepest parts of faults accelerate fluid flow. In the Model M10 (figure III.14), the fault is mineralized from 8 to 10.1 Myr, but does not change drastically the R^2AI distribution around the apex which appears to be the major control. In the model M11, the probable zone emerges after 1 Myr of emplacement within the fault closer to pluton where the hot fluid migrates far from the pluton. After 2.5 Myr of emplacement, this zone grows downward within the deeper part of the fault, where the permeability of fault is higher than the permeability of host rock (figure III.14). At the hottest phase, another zone appears at the surface near the fault where the permeability of host rock becomes higher than the fault. This zone disappears immediately at cooling period, while the zone inside fault vanishes after $8 \cdot 10^5$ years of cooling. The M11 pluton roof is emplaced at 5 km, i.e. between M2 and M3. Comparison between these models at the hottest phase (figure

6) shows that the flat lying fault has a major effect on the fluid flow pattern and the resulting R^2AI distribution. Indeed, the fault cancels the development of potential zone around the pluton. A very good agreement was found with the Crocetta deposit in Elba (figure 1D). The Elba central detachment fault is a very efficient advective drain. Indeed, due to its low dip, it is able to pump and accelerate the fluids at depth and make them circulate along the horizontal branch of the pluton-induced convection cells. This constitutes an important difference with high angle dip fault (as in M10). Detachments are then able to delocalize and strongly modifies classical fluid flow pattern induced by coeval intrusion.

7.5 Validity of modeled mineralization pattern

The essential point to discuss is the significance and reality of the near surface favourable zone developed above the pluton at the hottest phase. This is particularly relevant for deep seated plutons (e.g. M2, M3, figure III.12). There are two main limitations; first, we approximated a homogeneous crust with a power-law variation of permeability with depth (Eq. 3). This approximation does not take into account the potential permeability barriers encountered in many orogenic hydrothermal systems (e.g. Sibson et al., 1988). Secondly, the R^2AI is a physical parameter that does not take into account the solute transport and chemical reaction. For those obvious reasons, interpretations have to be very carefully proposed. However, we think that the near surface potential zone observed in models is not totally unreasonable. In fact, rather than ore deposits, it may correspond to geothermal systems with hot springs associated with deep heat sources, and more generally to alteration zones where large amount of hot fluids are efficiently cooled down (Hall et al., 1974).

7.6 Model time evolution vs. age of mineralization and genetic link

Because R^2AI is a pure physical parameter, the evolution of mineralization potential through time is not described over short time intervals; a more detailed time stepping would be required. Therefore our modeling is not able to reproduce the very short radiometric time span measured in ore deposits. This assumption is particularly valid for the Kucing Liar skarn (along the Indenberg fault) and the Grasberg Cu-Au porphyry (figure III.1C) which formed during 4.10^5 years time span. As analogue, the model M10 at 8 Myr (figure III.14) points out that both the Indenberg fault and the porphyry are potential favorable zones at the same time before the hottest phase. However, our simulations show that, without taking into account chemical processes, a pure physical parameter such as R^2AI applied to models of granite-related gold deposits (M6 and M8, figure III.13) reproduces correctly in time and space the ore deposition pattern relative to the pluton.

Indeed, the convection of fluids induced by the intrusion appears to be a key physical control to explain the spatial distribution of ore around the magmatic body.

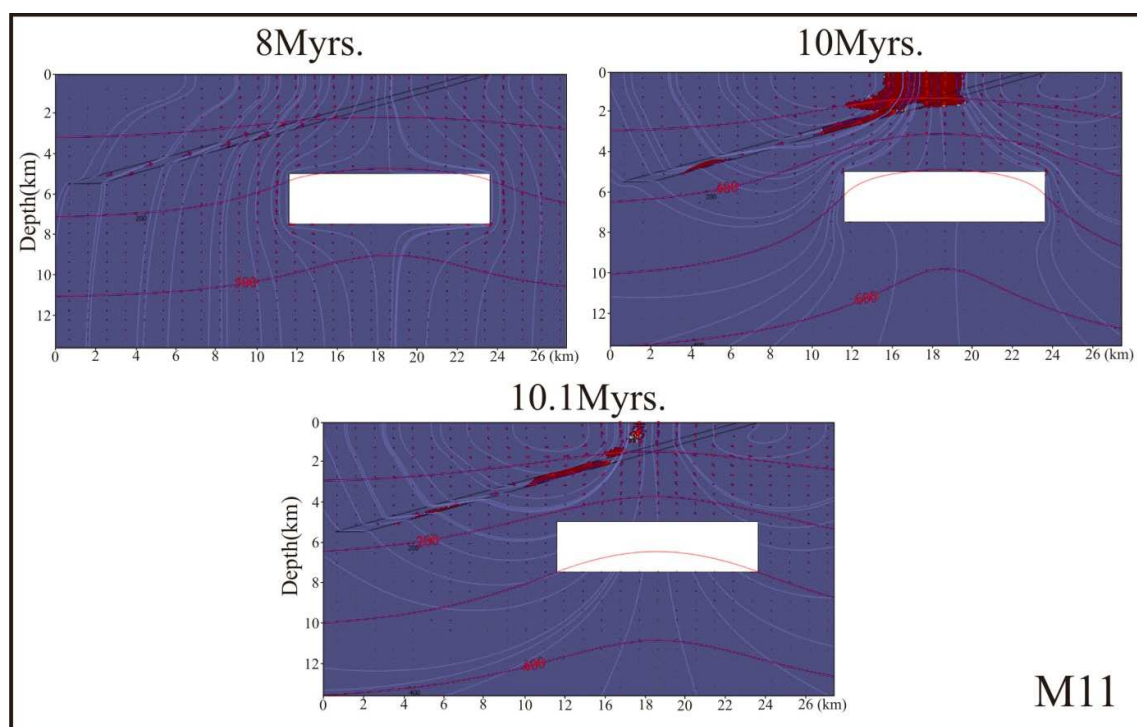
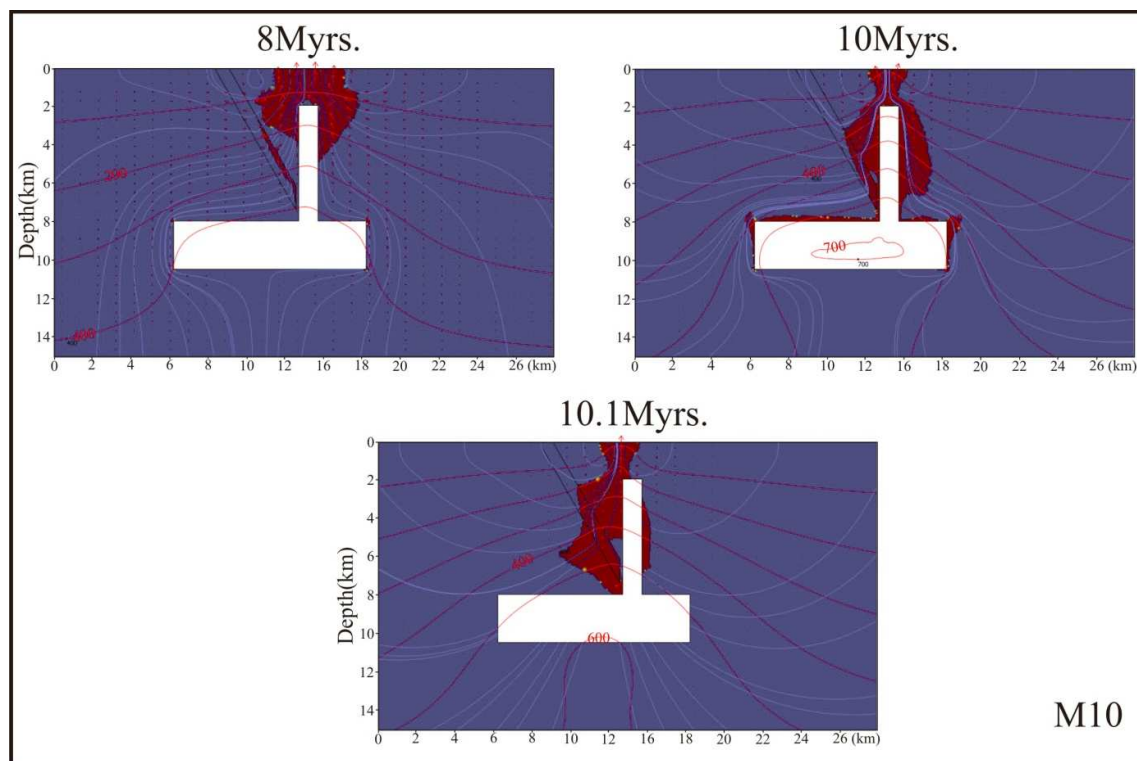


Figure (III.14): Same as Figure (III.13), M10 and M11 are simplified numerical models of the Grasberg porphyry and the Crocetta raw material deposits above the Elba detachment fault, respectively (see Figure 1 for geologic contexts).

This is valid because cracked thermal aureoles developed around the intrusion and focused the advective fluid flux (figure III.13). For M6 and M8, favourable zone developed from 9.5 Myr to 10.1 Myr (i.e. 6.10^5 years around the hottest phase figure III.13). This time span is shorter than the 2 Myr spanning granite emplacement and the mineralization events at Scheelite dome (cf. above). As it is emphasized in the introduction, fluid inclusion studies do not provide strong chemical arguments for a genetic link between granite and mineralization. Based on this lack of chemical evidences (e.g. no brines in fluid inclusions), granite is often only interpreted as a rheological and structural trap with no direct genetic relationships with ore deposition; even if radiometric time span between granite crystallization and mineralization is lower than 2 Myr. Our models show that from a physical point of view, hydrothermal convection created by magma emplacement is able to develop probable mineralized zone. The role of intrusion is then clearly genetic for this kind of the deep-seated granite-related Au deposits; and mineralization deposition might be nearly coeval with the hottest phase of intrusion.

8. Concluding remarks

Our models are simple physical models that do not simulate i) multiphase fluids; ii) chemical diffusion, iii) topography, iv) input of meteoric waters. Nevertheless, the originality of our modelling relatively to pre-existing works is: i) we varied continuously the crust permeability with depth; ii) models are transient and account for the emplacement period of intrusion, iii) we tested the physical favorability of ore deposition, iv) we compared with well-constrained natural examples at different emplacement depth with contribution of high permeability zones as cracked thermal aureoles and faults, v) the pluton floor zone has been explored.

Our main results are:

1. Fluid circulation and mineralization patterns are strongly dependent of the emplacement depth of the pluton. Deep seated plutons emplaced below 10 km and not connected to high permeability zones do not induce advective heat dissipation. Above 4.5 km of emplacement depth, the permeability threshold of 10^{-16} m^2 is reached and second order convection cells may create additional focused discharge zones where mineralization are expected.
 2. For all emplacement depth, the pluton floor zone is not favorable for mineral deposition.
 3. The apexes strongly modify the fluid flow pattern by focusing convective fluids and mineralization zones around them and depleting the main pluton of these fluids.
-

4. The cooling phase is not the main phase of convection for large pluton associated with long-lived magma emplacement. Major advective heat dissipation and mineral deposition zone may also occur sometime before and during the hottest phase of emplacement, before magma crystallizes. This is an important clue to interpret dating (emplacement, cooling age) of thermal aureole and intrusion-related ore deposits.
5. Detachment faults are able to delocalize and strongly modify classical fluid flow pattern induced by coeval intrusion. Extensional systems do not require lithostatic fluid overpressure to develop dilatant sites susceptible to drain and/or to trap mineralizations. This result implies that it is surprising that very few ore deposits are recognized in context of the detachments associated with metamorphic core.
6. Favorable physical conditions for mineral deposition are encountered around mid-crust pluton, during a short time span bracketing the hottest phase of intrusion. We conclude that even if chemical processes are absent from our models, fluid circulation induced by granite emplacement plays a key role in the genesis of granite-related Au deposits. Moreover, formation of this type of deposit is promoted and controlled by the occurrence of a fractured thermal aureole around the intrusion.

9. References

- Annen, C., Scaillet, B., Sparks, S.J., 2006. Thermal constraints on the emplacement rate of a large intrusive complex: the Manaslu Leucogranite, Nepal Himalaya. *Journal of Petrology*. 47, 71-95.
- Arndt, N.T., Leshner, C.M., Czamanske, G.K., 2005. Mantle-derived magmas and magmatic Ni–Cu–(PGE) deposits. *Economic Geology*. 100th Anniversary Volume, 5–24.
- Baker, T., Lang, J.R., 2001. Fluid inclusion characteristics of intrusion-related gold mineralization, Tombstone-Tungsten magmatic belt, Yukon territory, Canada. *Mineralium Deposita*. 36, 563-582.
- Bouillin, J.P., Bouchez, J.L., Lespinasse, P. Pêcher, A., 1993. Granite emplacement in an extensional setting: an AMS study of the magmatic structures of Monte Capanne (Elba, Italy). *Earth and Planetary Science Letters*. 118, 263-279.
- Cathles, L.M., 1977. An analysis of cooling of intrusives by ground-water convection which includes boiling. *Economic Geology*. 72, 804-826.
- Cathles, L.M., 1981, Fluid flow and genesis of hydrothermal ore deposits. *Economic Geology*. 75, 424-457.

- Cerny, P., Blevin, P.L., Cuney, M., London, D., 2005. Granite-related ore deposits In: Hedenquist JW, Thompson JFH, Goldfarb RJ, Richards JP (eds) One hundredth Anniversary Volume 1905-2005. Society of Economic Geologists. 100th Anniversary, 337-370.
- Clemens, J.D., Mawer, C.K. 1992. Granitic magma transport by fracture propagation. *Tectonophysics*. 204, 339-360.
- Cook, S.J., Bowman, J.R., Forster, G.B., 1997. Contact metamorphism surrounding the Alta stock: finite element model simulation of heat- and $^{18}\text{O}/^{16}\text{O}$ mass-transport during prograde metamorphism. *American Journal of Science*. 297, 1-55.
- Cui, X., Nabelek, P.I., Liu, M., 2001. Controls of layered and transient permeability on fluid flow and thermal structure in contact metamorphic aureoles, with application to the Notch Peak aureole, Utah. *Journal of Geophysical Research*. 106, 6477-6491.
- De Launay, L., 1913. *Traité de Minéralogie. Gîtes minéraux et métallifères*. Beranger, Paris.
- Dipple, G.M., Ferry, J.M., 1996. The effect of thermal history on the development of mineral assemblages during infiltration-driven contact metamorphism. *Contributions to Mineralogy and Petrology*. 124: 334.
- Driesner, T., Geiger, S., 2007. Numerical simulation of Multiphase Fluid Flow in Hydrothermal Systems. *Reviews in Mineralogy & Geochemistry*. 65, 187-212.
- Ferry, J.M., Dipple, G.M., 1992. Models for coupled fluid flow, mineral reaction, and isotopic alteration during contact metamorphism: The Nitch Peak aureole, Utah. *American Mineralogist*. 77, 577-591.
- Ferry, J.M., Sorensen, S.S., Rumble, D., 1998. Structurally controlled fluid flow during contact metamorphism in the Ritter Range pendant. California, USA. *Contributions to Mineralogy and Petrology*. 130, 358.
- Ferry, J.M., Wing, B., Penniston-Dorland, S., Rumble, D., 2002. The direction of fluid flow during contact metamorphism of siliceous carbonate rocks: new data for the Monzoni and Predazzo aureoles, northern Italy, and a global review. *Contributions to Mineralogy and Petrology*. 142, 679.
- Gerdes, M.L., Baumgartner, L.P., Person, M. 1998. Convective fluid flow through heterogeneous country rocks during contact metamorphism. *Journal of Geophysical Research* 103(B10), 23,983-24,003.

- Gloaguen, E., Chauvet, A., Branquet, Y., Gerbeaud, O., Ramboz, C., Bouchot, V., Lerouge, C., Monié, P., Cathelineau, M., Boiron M.C., Marignac, C., Pourraz, N., Fourcade, S., Ruffet, G., Iglesias Ponce de León, M., 2003. Relations between Au / Sn-W mineralizations and late Hercynian granite: Preliminary results from the Schistose Domain of Galicia-Trás-os-Montes Zone, Spain 7th biennial SGA meeting - Mineral Exploration and Sustainable Development. Athens, Greece, 271-274.
- Gloaguen, E., 2006. Apports d'une étude intégrée sur les relations entre granites et minéralisations filoniennes (Au et Sn-W) en contexte tardi-orogénique (Chaîne Hercynienne, Galice Cnentrale, Espagne) unpublished PhD Thesis, Orléans University, France, http://tel.archivesouvertes.fr/index.php?halsid=cu41odhccmgnb1qt3rek911j61&view_this_doc=tel-00107391&version=1, pp 571.
- Gow, P.A., Upton, P., Zhao, C., Hill, K.C., 2002. Copper-gold mineralisation in New Guinea: numerical modelling of collision, fluid flow and intrusion-related hydrothermal systems. *Australian Journal of Earth Sciences*. 49, 753-771.
- Guillou-Frottier, L., Burov, E.B., Milesi, J.-P., 2000. Genetic links between ash-flow calderas and associated ore deposits as revealed by large-scale thermo-mechanical modelling, *Journal of Volcanology and Geothermal Research*, 102, 339-361.
- Hall W.E., Friedman I. & Nash J.T. 1974 Fluid inclusion and light stable isotope study of Climx molybdenum deposits, Colorado. *Econo. Geol.* 69. 884-901.
- Hanson, R.B., 1995. The hydrodynamics of contact metamorphism. *Geological Society of America Bulletin*. 107, 595-611.
- Hanson, R.B., 1992. Effects of fluid production on fluid flow during regional and contact metamorphism. *Journal of Metamorphic Geology*. 10, 87-97.
- Harcouët, V., 2005. Modélisations thermiques de gisements orogéniques mésothermaux: application au Ghana, PhD Thesis, Institut de Physique du Globe de Paris, 266 pp.
- Ingebritsen, S.E., Manning, C.E., 1999. Geological implication of a permeability-depth curve for the continental crust. *Geology*. 27, 1107-1110.
- Lang, J.R., Baker, T., 2001. Intrusion-related gold systems: the present level of understanding. *Mineralium Deposita*. 36, 477-489.
- Lowell, J.D., Guilbert, J.M., 1970. Lateral and vertical alteration – mineralization zoning in porphyry ore deposits. *Economic Geology*. 65, 373-408.

- Maineri, C., Benvenuti, M., Costagliola, P., Dini, A., Lattanzi, P., Ruggieri, G., Villa, I.M., 2003. Sericitic alteration at the La Crocetta deposit (Elba Island, Italy): interplay between magmatism, tectonics and hydrothermal activity. *Mineralium Deposita*. 38, 67-86.
- Mair, J.L., Goldfarb, R.J., Johnson, C.A., Hart, C.J.R., Marsh, E.E., 2006. Geochemical Constraints on the Genesis of the Scheelite Dome Intrusion-Related Gold Deposit, Tombstone Gold Belt, Yukon, Canada. *Economic Geology*. 101, 523-553.
- Manning, C.E., Ingebritsen, S.E. 1999. Permeability of the continental crust: implications of geothermal data and metamorphic systems. *Reviews of Geophysics*. 37, 127-150.
- Nabelek, P.I., Labotka, T.C., 1993. Implications of geochemical fronts in the Notch Peak contact-metamorphic aureole, Utah, USA. *Earth and Planetary Science Letters*. 119, 539.
- Norton, D., Knapp, R., 1977. Transport phenomena in hydrothermal systems: the nature of porosity. *American Journal of Science*. 277.
- Norton, D., Knight, J., 1977. Transport phenomena in hydrothermal systems: cooling plutons. *American Journal of Science*. 277, 937-981.
- Oliver, N.H.S., McLellan, J.G., Hobbs, B.E., Cleverley, J.S., Ord, A., Feltrin, L. 2006. Numerical models of extensional deformation, heat transfer, and fluid flow across Basement-Cover interfaces during Basin-related Mineralization. *Economic Geology*. 101, 1-31.
- Petford, N., Cruden, A.R., McCaffrey, K.J.W., Vigneresse, J-L. 2000. Granitic magma formation, transport and emplacement in the Earth's crust. *Nature*. 408, 669-673.
- Phillips, O.M., 1991. *Flow and reactions in permeable rocks*. Cambridge University Press, Cambridge. 285pp.
- Pollard, P.J., Taylor, R.G., Peters, L., 2005. Ages of Intrusion, Alteration, and Mineralization at the Grasberg Cu-Au Deposit, Papua, Indonesia. *Economic Geology*. 100, 1005-1020.
- Rabinowicz M. Boulègue J. & Genthon P. 1998 Two and three-dimensional modeling of hydrothermal convection in the sedimented Middle Valley segment, Juan de Fuca Ridge. *J. Geophys. Res.*, 103, No. B10. 24045-24065.
- Raffensperger, J.P., Vlassopoloulos, D., 1999. The potential for free and mixed convection in sedimentary basins, *Hydrogeology Journal*, 7, 505-520.

- Rossetti, F., Tecce, F., Billi, A., Brilli, M., 2007. Patterns of fluid flow in the contact aureole of the Late Miocene Monte Capanne pluton (Elba Island, Italy): the role of structures and rheology. *Contributions to Mineralogy and Petrology*, 153, 743.
- Seedorf, E., Dilles, J.H., Proffett, J.M.J., Einaudi, M.R., Zurcher, L., Stavast, W.J.A., Johnson, D.A., Barton, M.D., 2005. Porphyry copper deposits: Characteristics and origin of hypogene features. *Economic Geology*, 100th Anniversary Volume, 251-298.
- Sibson, R.H., Robert, F., Poulsen, H.H.A.F., 1988. High angle faults, fluid pressure cycling, and mesothermal gold-quartz deposits. *Geology* 16, 551-555.
- Sillitoe, R.H., 1991. Intrusion-related gold deposits In: Foster RP (ed) *Gold metallogeny and exploration*. Blackie, Glasgow, 165-209.
- Stephens, J.R., Mair, J.L., Oliver, N.H.S., Hart, C.J.R., Baker, T., 2004. Structural and mechanical controls on intrusion-related deposits of the Tombstone Gold Belt, Yukon, Canada, with comparisons to other vein-hosted ore-deposit types. *Journal of Structural Geology*. 26, 1025-1041.
- Stern, L.A., Chamberlain, C.P., Barnett, D.E., Ferry, J.M., 1992. Stable isotope evidence for regional-scale fluid migration in a Barrovian metamorphic terrane, Vermont, USA. *Contributions to Mineralogy and Petrology*, 112: 475.
- Thompson, J.F.H., Sillitoe, R.H., Baker, T., Lang, J.R., Mortensen, J.K., 1999. Intrusion-related gold deposits associated with tungsten-tin provinces. *Mineralium Deposita*. 34, 323-334.
- Thompson, J.F.H., Newberry, R.J., 2000, Gold deposits related to reduce granitic intrusions In: Hagemann SG, Brown PE (eds) *Gold in 2000. Reviews in Economic Geology*. Society of Economic Geologists, Littleton, CO, USA, pp 377-400.
- Wing, B.A., Ferry, J.M., 2002. Three-dimensional geometry of metamorphic fluid flow during Barrovian regional metamorphism from an inversion of combined petrologic and stable isotopic data. *Geology*. 30, 639-642.
- Zhao, C., Hobbs, B.E., Mühlhaus, H.B., 1998. Finite element modelling of temperature gradient driven rock alteration and mineralization in porous rock masses. *Computer Methods in Applied Mechanics and Engineering*. 165, 175-187.
- Zhao, C., Hobbs, B.E., Walshe, J.L., Mühlhaus, H.B., Ord, A., 2001b. Finite element modeling of fluid-rock interaction problems in pore-fluid saturated

hydrothermal/sedimentary basins, *Computer Methods in Applied Mechanics and Engineering* 190, 2277-2293.

Zhao, C., Ge Lin, Hobbs, Ord, A., Yuejun Wang, B.E., Mühlhaus, H. B. 2003. Effects of hot intrusions on pore fluid flow and heat transfer in fluid-saturated rocks, *Computer Methods in Applied Mechanics and Engineering*.192, 2007-2030.

Table (III.1): Units and symbols of parameters and variables used in this study.

<i>Parameter</i>	<i>Unit</i>	<i>symbol</i>
<i>Fluid velocity</i>	$m.s^{-1}$	u
<i>Permeability</i>	m^2	K
<i>Dynamic viscosity</i>	$Pa.s$	μ
<i>Fluid density</i>	$Kg.m^{-3}$	ρ_f
<i>Fluid pressure</i>	Pa	P
<i>Gravitational acceleration</i>	$m.s^{-2}$	g
<i>Depth</i>	m	z
	km	Z
<i>Volumetric coefficient of thermal expansion</i>	K^{-1}	α_v
<i>Weighted average volumetric heat capacity</i>	$J.m^{-3}.K^{-1}$	C_{eq}
<i>Specific heat capacity</i>	$J.kg^{-1}.K^{-1}$	C_p
<i>Thermal conductivity</i>	$W.m^{-1}.K^{-1}$	λ

<i>Equivalent thermal conductivity</i>	$W.m^{-1}.K^{-1}$	λ_{eq}
<i>General heat source</i>	$W.m^{-3}$	Q
<i>Volumetric heat capacity of moving fluid</i>	$J.m^{-3}.K^{-1}$	C_L
<i>Temperature</i>	K, °C	T
<i>Porosity, (5% in pluton and host rocks)</i>	–	ϕ

10. Supplementary results

The results presented here focus on the effects of pluton geometry on distribution and magnitudes of temperature and fluid velocity in the host rock, (as they are for us the main factors controlling the probable zone of mineralization R²AI). We display the results for few relatively simple plan view geometries (horizontal rectangular, circular, square and tabular forms). The initial and boundary conditions were the same as those for the previous models.

The figure (III.15) illustrates the intrusion and the entire model domain. Black streamlines represent fluid velocities. Temperatures are shown with contour lines, which are roughly elliptical for all cases. As time progresses and distance from intrusion increases these contours become more flat. In all cases, two convective cells were located above the pluton corners near the topographic surface; the distance between them was controlled by the width of pluton.

To examine the effect of pluton shape on temperature and fluid velocities, we have drawn all pluton tops at constant depth (5km) with a constant surface area and we have made a cross section 1km above the pluton tops. Figure (III.16) shows temperature and fluid velocity curves evolution along the cross section. Thermal contours show that the tabular-like shape can heat a horizontal area larger than those heated by other shapes. As a result, the tabular shape can add 300C° to the area located 1km above the pluton. In contrast, the circular shape intruded the smallest horizontal plan in the host rock; therefore, the temperature does not rise significantly before and during emplacement.

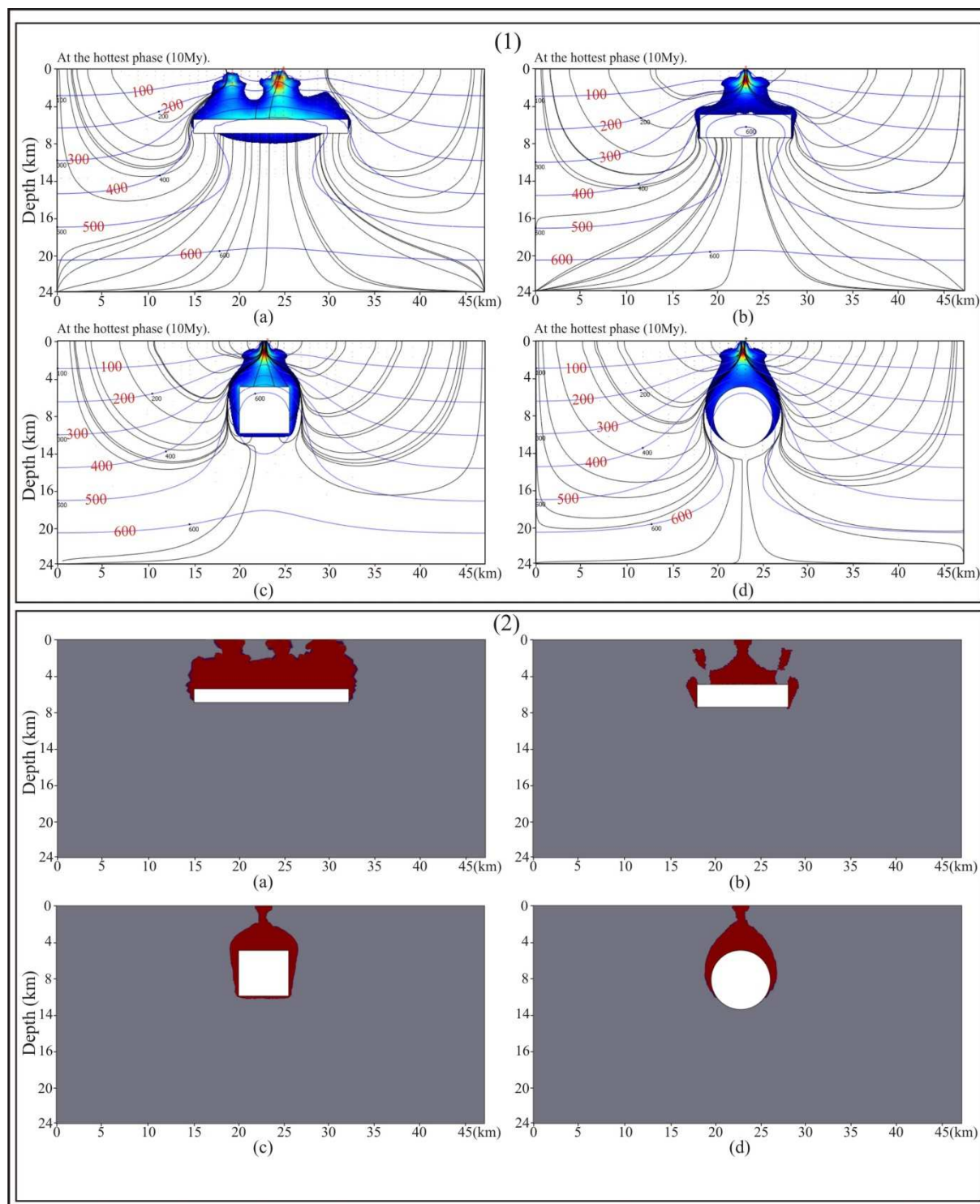


Figure (III.15): Four different shapes of pluton emplaced at the same depth, (1) the application of Peclet Number shows that the tabular-like form creates an advective zone (white zone represents the conductive zone

where P . Number is less than 1, while the coloured zone represents the advective zone where P . Number is equal or more than 1) larger than the other forms (blue lines represent the iso-thermal contours, and black lines represent the streamlines of fluid flow). (2) The application of RA^2I shows again that the tabular-like form produces a probable zone for mineralization wider than other geometries.

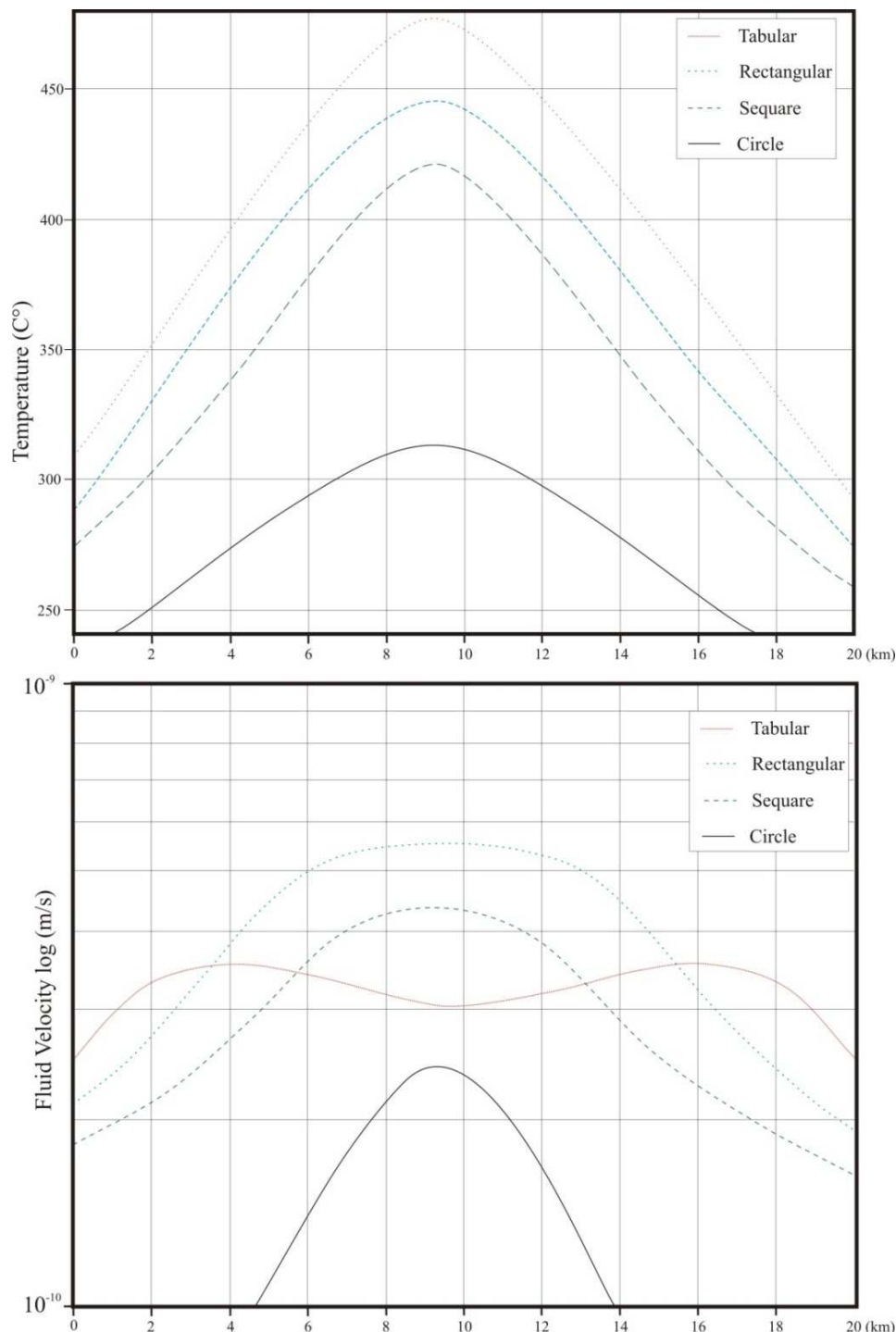


Figure (III.16): Temperature and fluid velocity curves at constant depth (1km above plutons), the results come from the models presented in figure 9. The curve which represents the fluid velocity above the tabular form shows two convective cells by two bulges and a depress of fluid velocities in x direction.

Here we do not discuss the effect of permeable zones (such as fractures and faults) which have a capacity to modify the permeability of host rock around intrusion. Therefore no significant effect of the shape was noticed in fluid velocity; we relate that to a constant permeability at each depth as we varied it vertically and not horizontally. In other words, the advected fluids could not circulate fast due to the vertical variation of permeability. This keeps hot fluids circulating slowly in deep zones because of the weak permeability. Multiple fractures around pluton could allow fluid to circulate faster and generate a more marked difference in fluid velocity (see previous results). The fluid velocity magnitudes also depend significantly on pluton geometry, but that is not observed here due to two reasons: a constant horizontal permeability and the emplacement depth of pluton (5km) which is considered as intermediate. These results show that, a great variety of additional factors, such as fracture system, spatial or temporal variations of material properties, varied horizontal permeability, shallow emplacement depth, more sophisticated geometry, can affect fluid velocities.

Moreover, the use of R^2 AI on these model outputs shows that the tabular shape is able to generate more favourable physical conditions for mineralization than other shapes, as it occupies more horizontal space. This conclusion is well supported by natural examples where mineralization is found near tabular pluton (e.g. Galicia, Spain, Gloaguen et al., 2006).